Multiwavelength observations reveal a faint candidate black hole X-ray binary in IGR J17285−2922

M. Stoop,[1]* J. van den Eijnden,[1] N. Degenaar,[1] A. Bahramian,[2,3] S. J. Swihart,[2,4]
J. Strader,[2] F. Jiménez-Ibarra,[5,6] T. Muñoz-Darias,[5,6] M. Armas Padilla,[5,6] A. W. Shaw,[7]
T. J. Maccarone,[8] R. Wijnands,[1] T. D. Russell,[1] J. V. Hernández Santisteban,[9]
J. C. A. Miller-Jones,[3] D. M. Russell,[10] D. Maitra,[11] C. O. Heinke,[12] G. R. Sivakoff,[12]
F. Lewis[13,14] D. M. Bramich[10]

[1]*Anton Pannekoek Institute for Astronomy, University of Amsterdam, Science Park 904, 1098 XH Amsterdam, the Netherlands*
[2]*Department of Physics and Astronomy, Michigan State University, East Lansing, MI 48824, USA*
[3]*International Centre for Radio Astronomy Research, Curtin University, GPO Box U1987, Perth, WA 6845, Australia*
[4]*National Research Council Research Associate, National Academy of Sciences, Washington, DC 20001, USA,*
  resident at Naval Research Laboratory, Washington, DC 20375, USA
[5]*Instituto de Astrofísica de Canarias (IAC), Vía Láctea s/n, La Laguna E-38205, S/C de Tenerife, Spain*
[6]*Departamento de Astrofísica, Universidad de La Laguna, La Laguna E-38205, S/C de Tenerife, Spain*
[7]*Department of Physics, University of Nevada, Reno, 1664 N. Virginia Street Reno, NV 89557, USA*
[8]*Department of Physics & Astronomy, Box 41051, Science Building, Texas Tech University, Lubbock, TX 79409-1051, USA*
[9]*SUPA Physics & Astronomy, University of St. Andrews, Fife, KY16 9SS, Scotland, UK*
[10]*Center for Astro, Particle and Planetary Physics, New York University Abu Dhabi, PO Box 129188, Abu Dhabi, UAE*
[11]*Department of Physics and Astronomy, Wheaton College, Norton, MA 02766, USA*
[12]*Department of Physics, CCIS 4-183, University of Alberta, Edmonton, AB, T6G 2E1, Canada*
[13]*Faulkes Telescope Project, School of Physics and Astronomy, Cardiff University, The Parade, Cardiff, CF24 3AA, Wales, UK*
[14]*Astrophysics Research Institute, Liverpool John Moores University, 146 Brownlow Hill, Liverpool L3 5RF, UK*

ABSTRACT

IGR J17285−2922 is a known X-ray binary with a relatively low peak 2–10 keV X-ray luminosity (1–2×10^{36} erg s^{-1} at 8 kpc) during outburst. Systems such as IGR J17285−2922 are of interest because we can study the physical reason for these X-ray binaries being so faint in the X-ray band and why only a few of these faint X-ray binaries, such as Swift J1357.2−0933 and XTE J1118+480, are known to harbour a black hole. IGR J17285−2922 went into a new outburst in 2019 after having exhibited two previous outbursts in 2003 and 2010. We have monitored this ∼ 4-month long 2019 outburst with *Swift* in X-ray and the Very Large Array in radio. In addition, we have obtained during this outburst four optical spectra with the Gran Telescopio Canarias and Southern Astrophysical Research Telescope, three optical photometry measurements with the Las Cumbres Observatory telescope network and one near-infrared spectrum with the Gemini South telescope. These observations are used to investigate the nature of the compact object, donor star and the orbital properties of the binary system. The ratio between its X-ray and radio luminosity is consistent with both samples of neutron star and black hole X-ray binaries, while the ratio between the X-ray and optical luminosity is consistent with black hole X-ray binaries. Studying the evolution of its X-ray power-law index Γ throughout the outburst, we find additional evidence for a black hole as compact object. The four optical spectra show no Hα emission and the nIR spectrum shows no Brγ emission, which suggests that the donor star could be hydrogen-poor and hence that IGR J17285−2922 might have an ultra-compact binary orbit. The shape of the X-ray light curve can be well described by an exponential, followed by a linear decay, from which we obtain a relation between the binary orbital period $P_{\rm orb}$ and the mass ratio q of the two binary components. We compare this relation to theoretical predictions and known ultra-compact X-ray binaries with constrained q and show that an ultra-compact binary orbit is possible for IGR J17285−2922. Lastly, we discuss how the observed properties of IGR J17285−2922 are reminiscent of short-$P_{\rm orb}$ black hole X-ray binaries.

Key words: X-rays:binaries – stars:individual:IGR J17285−2922 – accretion,accretion discs

1 INTRODUCTION

X-ray binaries are bright X-ray point sources. In an X-ray binary a compact object, a neutron star (NS) or black hole (BH), accretes matter from a stellar binary companion (donor star). Focusing on X-ray binaries with a low mass donor star ($\lesssim 1 M_\odot$), mass transfer to the compact object typically occurs through Roche-lobe overflow (Shakura & Sunyaev 1973). One class of such X-ray binaries are the so-called transient systems, which are mostly in a quiescent state during which (almost) no accretion onto the compact object takes place (typically lasting years), but sporadically show a bright X-ray outburst state (typically lasting weeks to months; Tetarenko et al. 2016).

During outburst, the accretion flow can transition to different states (see e.g. Remillard & McClintock 2006; Belloni 2010). Two main states that can be identified are the hard and soft state. During the soft state, the X-ray spectrum is dominated by low energy emission, while during the hard state the emission is dominated by high energy emission. In the hard state, the X-ray binary can launch part of the accreted material in the form of a collimated jet (Spencer 1979; Fender 2006). While the accretion flow is most prominently detected in the X-ray band up to optical, the jet is detected in radio and possibly also in (near-)infrared and optical (Russell et al. 2006, 2007). The matter in the jet is thought to arise from, and thus be correlated to, the accretion flow. For example, the study of X-ray binaries in the hard state in radio and X-ray simultaneously has revealed a coupling between this in- and outflow (see e.g. Corbel et al. 2003, 2013; Gallo et al. 2014, 2018).

The outburst-quiescence accretion cycles in transient X-ray binaries can be described by a disc instability model. As matter from the donor star builds up in the accretion disc during quiescence, a thermal instability eventually leads to an outburst with an increased mass accretion rate onto the compact object (see e.g. Lasota 2001; Hameury 2019). Transient X-ray binaries can be loosely classified based on the 2–10 keV peak X-ray luminosity during outburst (Wijnands et al. 2006). The 'bright X-ray binaries' reach peak luminosities of 10^{38}–10^{39} erg s^{-1}. However, not all X-ray binaries are this bright. Systems that have a peak luminosity of 10^{36}–10^{37} erg s^{-1} are typically called 'faint X-ray binaries'. Other X-ray binaries are even fainter, with peak luminosities of 10^{34}–10^{36} erg s^{-1}, which are called 'very faint X-ray binaries' (VFXBs). This faintness makes VFXBs hard to detect, with outbursts that may go unnoticed by X-ray all-sky monitors given their typically low resulting fluxes.

Three promising explanations have been proposed to account for the faint nature of these VFXBs. The first hypothesis is that VFXBs harbour NSs that truncate the accretion disc with their relatively strong magnetic field (Illarionov & Sunyaev 1975; Heinke et al. 2015). This prevents efficient accretion onto the NS, making the system faint in the X-ray band. It could also be possible for such systems to display a propeller driven outflow (D'Angelo & Spruit 2010). To identify a truncation of the inner disc, X-ray reflection spectroscopy can be used to measure the inner disc radius (Fabian et al. 1989). Although there are indications of a truncated disc in some VFXBs, distinguishing a magnetically-truncated disc from the formation of a radiatively-inefficient accretion flow in the disc has proved difficult (Narayan & Yi 1994; Degenaar et al. 2017; van den Eijnden et al. 2018).

The second hypothesis is that of ultra-compact X-ray binaries (UCXBs; King & Wijnands 2006; Heinke et al. 2015). The orbital period (P_{orb}) of such systems is typically defined as $\lesssim 90$ min (Nelson et al. 1986), which requires the donor star to be hydrogen poor to still fit within its Roche-lobe. Ultra-compact X-ray binaries can have

significantly reduced mass transfer rates, making the system faint in the X-ray band. A UCXB can be identified by directly measuring P_{orb} (e.g. measuring periodic eclipses or dips in X-ray or optical, or measuring periodic orbital modulations from optical photometry), indirectly using the requirement of a small accretion disc (e.g. using the ratio of optical to X-ray flux), or other diagnostics such as estimating the composition of the donor through spectral data [for a list of methods see e.g. in't Zand et al. (2007)]. One of these diagnostics involves the absence of Hα in optical spectra, as this may indicate a hydrogen-poor disc and therefore a hydrogen-poor donor star (Nelemans et al. 2004; Werner et al. 2006; Hernández Santisteban et al. 2019). Several UCXBs have been confirmed so far (e.g. Cartwright et al. 2013; Koliopanos et al. 2020 and references therein). The known sample of UCXBs consists (mostly) of NS accretors; BH UCXBs may have been identified in the extragalactic globular cluster NGC 4472 (Maccarone et al. 2007; Zepf et al. 2008; Steele et al. 2014) and a galactic BH UCXB may have been identified in 47 Tuc X9 (Miller-Jones et al. 2015; Bahramian et al. 2017).

The third hypothesis is that of symbiotic X-ray binaries. In this scenario, the compact object accretes matter from the wind of a giant donor star (see e.g. Masetti et al. 2006; Mattana et al. 2006; Masetti et al. 2007). Due to the low mass transfer rate from the giant donor star to the compact object, the system can be faint in the X-ray band. Recently, it was suggested that symbiotic X-ray binaries may contribute a significant fraction to the total population of VFXBs (Bahramian et al. 2020; Shaw et al. 2020).

Several other explanations have been put forward. VFXBs could be seen edge-on, making them appear fainter at such a high inclination. This can (possibly) be seen in systems such as CX-OGC J174540.0–290031 (Porquet et al. 2005; Muno et al. 2005) and Swift J1357.2–0933 (Corral-Santana et al. 2013; Mata Sánchez et al. 2015). VFXBs could arise from the so-called period gap X-ray binaries, in which the compact object captures the wind from a detached M dwarf donor star (Maccarone & Patruno 2013; Heinke et al. 2015). VFXBs could also simply be intrinsically bright systems at large distances (Wijnands et al. 2006). A single explanation for the nature of all VFXBs is unlikely, the class of VFXBs is likely to be heterogeneous.

VFXBs are interesting for multiple reasons. First, VFXBs allow an in-depth study of low-level accretion and this has revealed a diagnostic that could allow us to distinguish between NS and BH X-ray binaries (Wijnands et al. 2015). Accompanying this with a simultaneous study of the jet can give insight into the coupling between the accretion flow and jet at relatively low accretion rates. Second, VFXBs are also important for understanding binary evolution and population synthesis (see e.g. Maccarone et al. 2015). A complete understanding of the evolution of mass-transferring binary systems has proved to be difficult to develop (see e.g. Paczyński 1971; Tauris & van den Heuvel 2006). Measuring properties such as P_{orb}, the masses of the individual binary components and the nature of the accreting compact object for VFXBs can improve our understanding of their binary evolution and how these systems can get so faint in the X-ray band. Finally, VFXBs with an ultra-compact binary orbit are thought to produce low-frequency gravitational waves. They are consequently interesting targets to study with future gravitational wave missions, such as the *Laser Interferometer Space Antenna* (Nelemans et al. 2001; Nelemans & Jonker 2010).

1.1 IGR J17285−2922

IGR J17285−2922 is a borderline faint to very-faint X-ray binary first detected in outburst by *International Gamma-Ray Astrophysics Laboratory* (*INTEGRAL*) in 2003, with a 20–150 keV X-ray luminosity of $L_X \sim 10^{36}$ erg s^{-1} for an assumed distance of 8 kpc due to the proximity to the Galactic Centre (Barlow et al. 2005). X-ray activity coinciding with the position of IGR J17285−2922 was detected with the *Rossi X-ray Timing Explorer* from an unidentified source named XTE J1728−295 in 2010 (Markwardt & Swank 2010). XTE J1728−295 was confirmed to be the same source as IGR J17285−2922 in subsequent observations with the *Neil Gehrels Swift Observatory* (*Swift*; Gehrels et al. 2004) and *INTEGRAL* (Yang et al. 2010; Turler et al. 2010). The search for the optical counterpart during this 2010 outburst resulted in the identification of a variable star with $R \sim 19$ mag and $I \sim 18.5$ mag (Russell et al. 2010a; Torres et al. 2010; Russell et al. 2010b). An in-depth investigation on this 2010 outburst was done by Sidoli et al. (2011) using a high quality *XMM-Newton* observation, along with *INTEGRAL* data. Sidoli et al. (2011) concluded that IGR J17285−2922 is a transient VFXB, although no definitive answer was found for the nature of the compact object. The absence of thermonuclear X-ray bursts and X-ray pulsations allowed for either a NS or BH primary (Sidoli et al. 2011).

More recently, on April 8–9, 2019, *INTEGRAL* found renewed X-ray activity from IGR J17285−2922 (Ducci et al. 2019). To further investigate its nature, we monitored this 2019 outburst in the X-ray band with *Swift* and in radio with the Karl G. Jansky Very Large Array (VLA). On top of this, we obtained throughout the outburst four optical spectra covering Hα with the Southern Astrophysical Research Telescope (SOAR) and Gran Telescopio Canarias (GTC), one near-infrared (nIR) spectrum with the Gemini South telescope and three optical photometry measurements with the Las Cumbres Observatory (LCO) telescope network. We will use these multi-wavelength observations to constrain the nature of the compact object, donor star, as well as the binary orbital properties of the (V)FXB IGR J17285−2922.

2 OBSERVATIONS AND ANALYSIS

2.1 X-rays

We monitored the outburst of IGR J17285−2922 with *Swift* to track the outburst evolution and the accretion state. Between April 10 (2 days after the initial *INTEGRAL* detection) and September 20, 2019, a total of 45 observations were taken (Target ID 00011287 and 00011303, see Table 1 for an overview) with the *Swift* X-ray Telescope (XRT; Burrows et al. 2005). These *Swift*/XRT observations had a typical duration of ~ 1 ks. Only the first observation was taken in Window Timing (WT) mode, while all other observations were taken in Photon Counting (PC) mode. We extracted the 0.3–10 keV count rates with the *Swift*/XRT product generator[1] (Evans et al. 2007, 2009). We calibrated the observations using the XRTPIPELINE (version 0.13.5) and the CALDB in the HEASOFT package (version 6.26.1) provided by HEASARC[2]. The images and spectra were extracted using XSELECT (version v2.4g). For the single WT observation (ObsID 00011287001), we used a circular source extraction region with a radius of 35″ and two circular background

---

[1] https://www.swift.ac.uk/user_objects/
[2] https://heasarc.gsfc.nasa.gov/

extraction regions with radii of 35″ each, placed sufficiently far away from the source. For the PC observations, we first correct for pile-up if needed. For the 2nd up to and including the 8th observations (ObsID 00011303002−00011303010), correction for pile-up was required and we used an annular source extraction region with an inner radius of 10″ and outer radius of 35″. For the 9th, 10th, 11th and 13th observation (ObsID 00011303011−00011303013 and 00011303015), correction for pile-up was also required and we used an annular source extraction region with an inner radius of 6″ and outer radius of 35″. For all other PC observations, we used a circular source extraction region with a radius of 25″. In all the PC observations, we used three circular background extraction regions with radii of 60″ each. The ancillary response files were created with the observation-specific exposure-maps using XRTMKARF (version 0.6.3). The response matrix files `swxwt0to2s6_20131212v015` and `swxpc0to12s6_20130101v014`, for WT and PC mode respectively, were obtained from the CALDB (version 20190412). All spectra were grouped to have a minimum of 1 count per bin with GRPPHA. On top of this we also grouped the first five spectra (ObsIDs 00011287001 and 00011303002−00011303005) separately to have a minimum of 20 counts per bin with GRPPHA.

We fitted the *Swift*/XRT spectra using XSPEC (v. 12.10.1f; Arnaud 1996). We used an absorbed powerlaw model (TBABS * POWERLAW) and a combined absorbed powerlaw plus blackbody model (TBABS * [BBODYRAD + POWERLAW]). We performed these fits with the hydrogen column density parameter (N_H in TBABS; Wilms et al. 2000) as three different options; N_H as a free parameter, fixed at $N_H = 0.51 \times 10^{22}$ cm^{-2} (Sidoli et al. 2011), and fixed at $N_H = 0.99 \times 10^{22}$ cm^{-2} (determined by the simultaneous fit of all *Swift*/XRT spectra with N_H tied for each spectrum). The impact of N_H on the determined spectral parameters is discussed in Section 4.5. We adopted the cross-sections by Verner et al. (1996) and abundances by Wilms et al. (2000). For consistency, and due to the low total counts in the last half of the outburst, the model fitting was done using Cash statistics (Cash 1979) in all spectra. In addition, we also used χ^2 statistics for the first five spectra to perform the F-test (see Section 3.3). The results using both Cash and χ^2 statistics were consistent with each other.

We determined the 0.5–10 keV and 1–10 keV unabsorbed fluxes with CFLUX. For radio epochs 1, 3 and 4 (see Section 2.2, no quasi-simultaneous *Swift*/XRT observations were taken. We determined the X-ray flux (1–10 keV) during these radio epochs using a linear interpolation between the closest *Swift*/XRT observations before and after each of these radio epochs. The two fluxes used for each interpolation are similar down to 30%. We use the largest positive and negative 1σ error of the interpolated X-ray fluxes for the 1–10 keV flux during each radio epoch. The 1–10 keV X-ray fluxes adopted during each radio epoch are listed in Table 2.

2.2 Radio

We monitored the 2019 outburst of IGR J17285−2922 with the VLA over 7 epochs (project code SF8027, see Table 2 for an overview). In epochs 1 to 4, the VLA observations were taken in the B configuration, in epochs 5 and 6 in a BnA configuration and in epoch 7 in the A configuration. In all epochs, IGR J17285−2922 was observed at C band in 8-bit mode, with two subbands at central frequencies of 4.5 and 7.5 GHz, with 1 GHz bandwidth each. The primary flux calibrator was 3C 286 = J1331+3030 and the secondary phase calibrator was J1743−3058 ($\sim 3.6°$ angular distance).

We analysed the observations using the Common Astronomy

Table 1. Overview of the *Swift*/XRT observations and spectral fits for the 2019 outburst of IGR J17285−2922. We used an absorbed powerlaw model with the hydrogen column density fixed at $N_H = 0.99 \times 10^{22}$ cm^{-2}. Γ gives the X-ray power-law index. For the non-detections as IGR J17285−2922 becomes quiescent, we assume that the spectra are equal to the last detected spectrum (ObsID 00011287002) to determine the 3σ upper limits on the 0.5–10 keV X-ray flux by scaling the count rates. All uncertainties are 1σ. Upper limits are 3σ. Fixed parameters are indicated with an asterisk.

	ObsID	Date	MJD	Count rate (cts s^{-1})	Γ	0.5–10 keV flux ($\times 10^{-12}$ erg cm^{-2} s^{-1})	C-stat / dof
1	00011287001	Apr 10, 2019	58583	3.2 ± 0.1	1.69 ± 0.08	152 ± 6	386 / 438
2	00011303002	Apr 15, 2019	58588	2.7 ± 0.1	1.61 ± 0.08	193 ± 8	270 / 352
3	00011303003	Apr 17, 2019	58590	2.6 ± 0.1	1.63 ± 0.07	191^{+8}_{-7}	345 / 386
4	00011303004	Apr 19, 2019	58592	2.2 ± 0.1	1.70 ± 0.08	154^{+7}_{-6}	282 / 326
5	00011303005	Apr 21, 2019	58594	2.2 ± 0.1	1.58 ± 0.08	154 ± 7	327 / 346
6	00011303008	Apr 29, 2019	58602	1.71 ± 0.07	1.47 ± 0.09	146 ± 7	245 / 306
7	00011303009	May 01, 2019	58604	1.73 ± 0.08	1.6 ± 0.1	110 ± 6	219 / 243
8	00011303010	May 03, 2019	58606	1.50 ± 0.08	1.53 ± 0.09	110 ± 6	216 / 286
9	00011303011	May 05, 2019	58608	1.20 ± 0.06	1.50 ± 0.09	97 ± 5	239 / 276
10	00011303012	May 07, 2019	58610	1.16 ± 0.05	1.53 ± 0.08	94^{+5}_{-4}	249 / 305
11	00011303013	May 09, 2019	58612	1.2 ± 0.1	1.5 ± 0.1	71 ± 5	135 / 189
12	00011303014	May 11, 2019	58614	1.05 ± 0.09	1.6 ± 0.1	70 ± 6	126 / 135
13	00011303015	May 13, 2019	58616	0.89 ± 0.06	1.34 ± 0.09	66 ± 4	209 / 278
14	00011303016	May 15, 2019	58618	0.77 ± 0.04	1.37 ± 0.08	60 ± 3	258 / 308
15	00011303017	May 17, 2019	58620	0.64 ± 0.04	1.25 ± 0.09	49 ± 3	201 / 293
16	00011303018	May 19, 2019	58622	0.74 ± 0.04	1.35 ± 0.09	55 ± 3	245 / 300
17	00011303019	May 23, 2019	58626	0.66 ± 0.05	1.3 ± 0.1	51 ± 3	187 / 239
18	00011303020	May 25, 2019	58628	0.59 ± 0.04	1.41 ± 0.09	44^{+3}_{-2}	229 / 269
19	00011303021	May 27, 2019	58630	0.50 ± 0.03	1.4 ± 0.1	41^{+3}_{-2}	163 / 250
20	00011303022	May 29, 2019	58632	0.55 ± 0.03	1.6 ± 0.1	42 ± 2	240 / 253
21	00011303023	May 31, 2019	58634	0.50 ± 0.03	1.6 ± 0.1	39 ± 2	167 / 254
22	00011303024	June 02, 2019	58636	0.46 ± 0.03	1.8 ± 0.1	36 ± 2	211 / 234
23	00011303025	June 04, 2019	58638	0.50 ± 0.03	1.37 ± 0.09	41 ± 2	210 / 287
24	00011303026	June 06, 2019	58640	0.44 ± 0.04	1.5 ± 0.2	27 ± 3	78 / 81
25	00011303027	June 08, 2019	58642	0.42 ± 0.03	1.5 ± 0.1	36 ± 2	254 / 252
26	00011303028	June 10, 2019	58644	0.46 ± 0.03	1.4 ± 0.1	36 ± 2	196 / 254
27	00011303029	June 19, 2019	58653	0.49 ± 0.03	1.47 ± 0.09	37 ± 2	228 / 274
28	00011303030	June 26, 2019	58660	0.57 ± 0.03	1.58 ± 0.09	46^{+3}_{-2}	183 / 261
29	00011303031	July 03, 2019	58667	0.33 ± 0.03	1.3 ± 0.1	28^{+3}_{-2}	125 / 136
30	00011303032	July 10, 2019	58674	0.45 ± 0.03	1.8 ± 0.1	32 ± 2	165 / 214
31	00011303033	July 17, 2019	58681	0.31 ± 0.02	1.5 ± 0.1	25 ± 2	137 / 187
32	00011303034	July 24, 2019	58688	0.23 ± 0.03	1.8 ± 0.3	16 ± 2	53 / 61
33	00011303035	July 31, 2019	58695	0.15 ± 0.02	1.7 ± 0.2	13^{+2}_{-1}	53 / 70
34	00011303036	Aug 07, 2019	58702	0.14 ± 0.01	1.4 ± 0.2	12 ± 2	72 / 70
35	00011287002	Aug 16, 2019	58711	0.031 ± 0.006	1.4 ± 0.5	$2.7^{+0.9}_{-0.6}$	30 / 20
36	00011287003	Aug 23, 2019	58718	< 0.02	1.4^*	< 1.6	-
37	00011287004	Aug 25, 2019	58720	< 0.009	1.4^*	< 0.8	-
38	00011287005	Aug 27, 2019	58722	< 0.009	1.4^*	< 0.8	-
39	00011287006	Aug 29, 2019	58724	< 0.007	1.4^*	< 0.6	-
40	00011287007	Aug 30, 2019	58725	< 0.01	1.4^*	< 1.2	-
41	00011287008	Sep 01, 2019	58727	< 0.009	1.4^*	< 0.8	-
42	00011287009	Sep 08, 2019	58734	< 0.007	1.4^*	< 0.6	-
43	00011287010	Sep 13, 2019	58739	< 0.01	1.4^*	< 1.2	-
44	00011287011	Sep 20, 2019	58746	< 0.02	1.4^*	< 2.0	-

Software Application[3] (CASA version 5.6.1; McMullin et al. 2007). Radio frequency interference and other data artifacts were removed by careful visual inspection, in combination with automated CASA routines. We imaged the calibrated 4–5 and 7–8 GHz Stokes I data separately using TCLEAN, with a Briggs weighting scheme robust parameter of 0, balancing sensitivity and the impact of other nearby sources. We determined the flux density in the image plane by fitting a 2D elliptical Gaussian using IMFIT, with the ellipse parameters fixed to those of the synthesized beam. We determined the 1σ error on the flux density by measuring the RMS of a nearby area containing no sources in the image plane. When the source was not detected in either the 4–5 or 7–8 GHz subband, we determined a 3σ upper limit as three times the RMS over the source location in the image plane. The details of the VLA observations are given in Table 2.

To determine the spectral index (α) of the radio emission, we performed Monte-Carlo (MC) simulations. For each radio epoch in which IGR J17285−2922 was detected in both the 4–5 and 7–8 GHz subband, we drew 10^6 frequencies between 4 and 5 GHz ($\nu_{4-5 \text{ GHz}}$) and between 7 and 8 GHz ($\nu_{7-8 \text{ GHz}}$) assuming a uniform distribution. For each of these individual frequencies, we drew

[3] https://casa.nrao.edu/

Table 2. Overview of the VLA observations for the 2019 outburst of IGR J17285−2922. The spectral index α for each VLA observation is calculated as described in Section 2.2. For each VLA observation, we give the (quasi-)simultaneous 1–10 keV X-ray flux and the *Swift*/XRT ObsID(s) used for this flux. *Swift*/XRT ObsID(s) followed by an asterisk indicate that the (quasi-)simultaneous 1–10 keV X-ray flux has been interpolated. Upper and lower limits are 3σ, while all uncertainties are 1σ.

	Date	MJD	Frequency (GHz)	Flux density (μJy)	Spectral index α	1–10 keV X-ray flux ($\times 10^{-12}$ erg cm^{-2} s^{-1})	*Swift*/XRT ObsID(s)
1	Apr 13, 2019	58586	4–5 / 7–8	118 ± 7 / 126 ± 5	0.1 ± 0.1	152^{+9}_{-8}	00011287001 - 00011303002*
2	Apr 19, 2019	58592	4–5 / 7–8	93 ± 10 / 102 ± 8	0.2 ± 0.3	129^{+7}_{-6}	00011303004
3	June 14, 2019	58648	4–5 / 7–8	< 33 / 80 ± 9	> 0.9	33 ± 2	00011303028 - 00011303029*
4	June 23, 2019	58657	4–5 / 7–8	81 ± 11 / 67 ± 9	-0.4 ± 0.4	37 ± 3	00011303029 - 00011303030*
5	July 11, 2019	58675	4–5 / 7–8	< 38 / 62 ± 10	> -0.2	27 ± 2	00011303032
6	July 30, 2019	58694	4–5 / 7–8	62 ± 12 / 46 ± 11	-0.6 ± 0.6	10^{+2}_{-1}	00011303035
7	Aug 15, 2019	58710	4–5 / 7–8	< 33 / < 30	-	$2.4^{+0.9}_{-0.7}$	00011287002

a flux density ($S_{4–5\,GHz}$ and $S_{7–8\,GHz}$) assuming a Gaussian distribution with mean and standard deviation equal to the observed flux density and RMS respectively. We determined α using $S_{7–8\,GHz} = S_{4–5\,GHz} \times (\nu_{7–8\,GHz} / \nu_{4–5\,GHz})^{\alpha}$. We determined α and 1σ errors, as the 50th, 16th and 84th percentile respectively. When IGR J17285−2922 was detected in only one subband, we determined a 3σ upper limit on α using the procedure described in van den Eijnden et al. (2019). In this procedure, an MC simulation is performed to determine at what α (3σ upper or lower limit) the non-detected subband would have been detected.

2.3 Optical photometry

We observed IGR J17285−2922 with the LCO 2-meter Faulkes and 1-meter network of telescopes during the 2019 outburst, as part of a monitoring campaign of ∼ 50 LMXBs (Lewis et al. 2008; Russell et al. 2010a,b). Imaging data were taken mostly in the Bessell *I* filter. The newly developed "X-ray Binary New Early Warning System" (XB-NEWS) pipeline (Russell et al. 2019) was used to compute astrometric solutions, perform multi-aperture photometry, and flux calibrate the photometry. The pipeline produces a calibrated light curve for the target (for more details see Russell et al. 2019; Goodwin et al. 2020). For images in which the target is not automatically detected above the detection threshold by the pipeline, XB-NEWS performs forced multi-aperture photometry at the known position of the source. All derived magnitudes with an uncertainty > 0.25 mag were considered unreliable, and were rejected.

2.4 Optical spectroscopy

We obtained four epochs of optical spectroscopy of IGR J17285−2922 during the outburst with the purpose of investigating the presence of Hα. We observed the target on the nights of April 30 – May 1, May 2–3, and June 29–30, 2019 with SOAR, using the Goodman Spectrograph (Clemens et al. 2004). The first two runs both consisted of two exposures of 1800 s each, using a 400

l/mm grating with a 0.95 arcsec slit, yielding a FWHM resolution of ∼ 5.6Å over the wavelength range from ∼ 3800–7800Å. The final run consisted of two 1500 s exposures, using the same grating on a 1.2 arcsec slit, resulting in a ∼ 7.6Å FWHM resolution between ∼ 4850–8850Å. The spectra were reduced and optimally extracted following standard practices using IRAF.

We also observed IGR J17285−2922 using the OSIRIS instrument (Cepa et al. 2000) mounted on the 10.4-meter GTC, on the night of July 21–22, 2019. We obtained two spectra with exposures times of 600 s each, using the grism R2500R (5575–7685 Å) with a 1 arcsec slit, providing a velocity resolution of 160 km s^{-1}. The data reduction and calibration was performed using IRAF, after which we used MOLLY and PYTHON routines to analyse, normalise, and plot the spectra.

2.5 nIR spectroscopy

On 2019 July 08 we obtained long slit spectroscopy of the nIR counterpart to IGR J17285−2922 with Flamingos-2 on the 8.1m Gemini South telescope at Cerro Páchon, Chile as part of program ID GS-2019A-FT-106 (PI: Shaw). We obtained 21x120 s exposures with the *HK* grism and a slit width of 2 pixels (0.''36) which provides a typical FWHM resolution of ∼ 24 Å at Brackett γ (Brγ; 2.166μm). To reduce the effect of the rapidly changing background at nIR wavelengths we dithered along the spatial directions of the slit in an ABBA pattern. On the same night we also used the same set up to observe the telluric standard star Hip 82714, obtaining 4x2 s images.

Data were reduced using the Gemini package in IRAF [4] following standard procedures. We normalised the averaged spectrum of the telluric standard star and removed the hydrogen Brackett-series absorption features by subtracting a best-fit Voigt profile. We then

---
[4] https://www.gemini.edu/observing/phase-iii/understanding-and-processing-data/data-processing-software/gemini-iraf-general

used the task `nstelluric` to shift and scale the science and telluric spectra in order to optimally divide out telluric features from the science spectra.

3   RESULTS

3.1   X-ray and radio light curves

We show the *Swift* and VLA light curve of the 2019 outburst of IGR J17285−2922 in Figure 1. The *Swift* light curve shows a globally decreasing count rate as the outburst proceeds, with a plateau between June 6 and July 6, 2019 (MJD 58640 and 58670, respectively). IGR J17285−2922 was first observed with *Swift* on April 10, 2019 (MJD 58583), and was last detected on August 16, 2019 (MJD 58711), for a total outburst duration of 128 days as observed with *Swift*. The 42nd *Swift*/XRT observation (MJD 58734) is reported as a detection by the *Swift*/XRT product generator (Evans et al. 2007, 2009), but manually analysing this observation with XIMAGE, with both DETECT and SOSTA, shows that IGR J17285−2922 is not detected at even 1σ confidence. Instead, we adopt a 3σ upper limit on the count rate for this observation by tripling the background count rate as determined with XSELECT.

We show the flux densities in the 4–5 and 7–8 GHz subbands of the VLA observations of IGR J17285−2922 in Figure 1, which are listed in Table 2. IGR J17285−2922 is detected during radio epochs 1, 2, 4 and 6 in both the 4–5 and 7–8 GHz subband with flux densities of $\sim$ 50–120 μJy and is consistent with a flat spectrum of $\alpha \sim -0.6$ to 0.2. However during radio epochs 3 and 5, the source is only detected in the 7–8 GHz subband, yielding 3σ lower limits on α of 0.9 and −0.2, respectively. During radio epoch 7, IGR J17285−2922 is no longer detected in either frequency subband with 3σ flux density upper limits of $\sim$ 30 μJy. This radio non-detection occurs around the time of a sharp decline in *Swift*/XRT count rate as IGR J17285−2922 becomes quiescent.

Using radio epoch 1 (7–8 GHz subband), with the highest signal-to-noise ratio (S/N), to determine the best-fit radio position gives

RA = $17^{\mathrm{h}}\, 28^{\mathrm{m}}\, 38.9^{\mathrm{s}} \pm 0.3^{\mathrm{s}}$

Dec = $-29° \, 21' \, 43.2'' \pm 0.1''$

Where the uncertainties are estimated from the astrometric accuracy of the VLA. Since the S/N is larger than 10 for epoch 1, we use 10% of the synthesised beam to determine the uncertainties. This position is fully consistent with the position determined with the *Chandra X-ray Observatory* during the 2010 outburst (Chakrabarty et al. 2010).

3.2   Radio/X-ray coupling

The coupling between the accretion flow and jet has revealed a difference between NS and BH X-ray binaries. In the radio/X-ray luminosity plane ($L_\mathrm{R} - L_\mathrm{X}$ plane), BH X-ray binaries have a (e.g. 5 GHz) radio luminosity that is typically a factor of $\gtrsim$ 10 greater than the radio luminosity of NS X-ray binaries at equal (e.g. 1–10 keV) X-ray luminosities (see e.g. Fender & Kuulkers 2001; Gallo et al. 2018). This difference is clearly visible in Figure 2, where we show the position of NS and BH X-ray binaries in the $L_\mathrm{R} - L_\mathrm{X}$ plane for 5 GHz radio luminosities and 1–10 keV X-ray luminosities (database[5] was consulted January 2020; Bahramian et al. 2018). We

can therefore use the (quasi-)simultaneous radio/X-ray observations of IGR J17285−2922 to determine whether these are consistent with the NS or BH X-ray binary samples to gain insight into the nature of the compact object.

In order to study the position of IGR J17285−2922 in the $L_\mathrm{R} - L_\mathrm{X}$ plane, we determine the 5 GHz radio- and 1–10 keV X-ray luminosities. The distance to IGR J17285−2922 has only been constrained to $d \gtrsim 4$ kpc, based on a non-detection ($R > 21$ mag) in an archival optical image (Sidoli et al. 2011). We adopt a range of distances of 4, 8, 12 and 16 kpc to investigate the nature of the compact object for each of these distances. The (quasi-)simultaneous 1–10 keV unabsorbed X-ray fluxes are determined with the method described in Section 2.1 and the best-fit model determined in Section 3.3. The 1–10 keV X-ray luminosities are consequently calculated with $L_{1-10\,\mathrm{keV}} = 4\pi d^2 F_{1-10\,\mathrm{keV}}$, where $F_{1-10\,\mathrm{keV}}$ are the unabsorbed 1–10 keV X-ray fluxes. The radio luminosities are calculated with $L_\nu = 4\pi d^2 \nu S_\nu$. The 4–5 and 7–8 GHz radio flux densities, along with the (quasi-)simultaneous 1–10 keV X-ray fluxes are given in Table 2.

Figure 2 shows IGR J17285−2922 (for assumed distances of 4, 8, 12 and 16 kpc) in the $L_\mathrm{R} - L_\mathrm{X}$ plane along with other NS and BH X-ray binaries. We show the 7–8 GHz instead of the 4–5 GHz radio luminosities assuming a flat spectrum to avoid cluttering, which is valid for all VLA observations except the third VLA observation with a strongly inverted spectrum ($\alpha > 0.91$). The results we obtain here from using the 7–8 GHz radio luminosities in Figure 2 are consistent with the results using the 4–5 GHz radio luminosities. For a distance of 4 kpc, the $L_\mathrm{R} - L_\mathrm{X}$ location of IGR J17285−2922 is more consistent with NS X-ray binaries. For increasing distances, the $L_\mathrm{R} - L_\mathrm{X}$ location of IGR J17285−2922 is consistent with both BH- and NS X-ray binaries. For a distance of 16 kpc and greater, the $L_\mathrm{R} - L_\mathrm{X}$ location of IGR J17285−2922 becomes more consistent with that of BH X-ray binaries. Without knowing the distance of IGR J17285−2922, we can thus not determine the nature of the compact object based on its location in the $L_\mathrm{R} - L_\mathrm{X}$ plane.

Our *Swift*/XRT observations sample a L_X range of nearly 2 orders of magnitude, allowing us to determine the correlation coefficient between L_R and L_X. We investigate the $L_\mathrm{R} - L_\mathrm{X}$ luminosity correlation using a linear fit in log-log space in the form of

$$\log(L_\mathrm{R}) - 28 = \delta + \gamma [\log(L_\mathrm{X}) - 35] + \epsilon. \qquad (1)$$

Here δ is the offset (scaling factor in linear space), γ is the slope of the line (power-law index in linear space) to be determined and ϵ is a Normal random variable representing the intrinsic random scatter about the regression line with mean equal to 0 and standard deviation σ_ϵ as a free parameter (Kelly 2007). Following Gallo et al. (2014) and Gusinskaia et al. (2020), we use the PYTHON port of LINMIX[6] method developed by Kelly (2007). In this method, Markov Chain Monte-Carlo (MCMC) simulations are performed to fit the linear model in Equation 1 taking upper limits on the data into account. The LINMIX performs a fit of the parameters γ, δ and σ_ϵ. We estimate γ, δ and σ_ϵ by calculating the mean for each parameter from the marginalised posterior distributions (100000 iterations) and determined the 1σ uncertainties on these parameters by taking the 16–84th percentile of the marginalised posterior distributions. We have performed this method for the 7–8 GHz radio flux densities and X-ray fluxes given in Table 2 (including the upper limit in radio in epoch 7), converted these to their respective luminosities as described above (for a distance of 8 kpc). Similar to Gallo et al.

---

[5] https://github.com/bersavosh/XRB-LrLx_pub

[6] https://github.com/jmeyers314/linmix
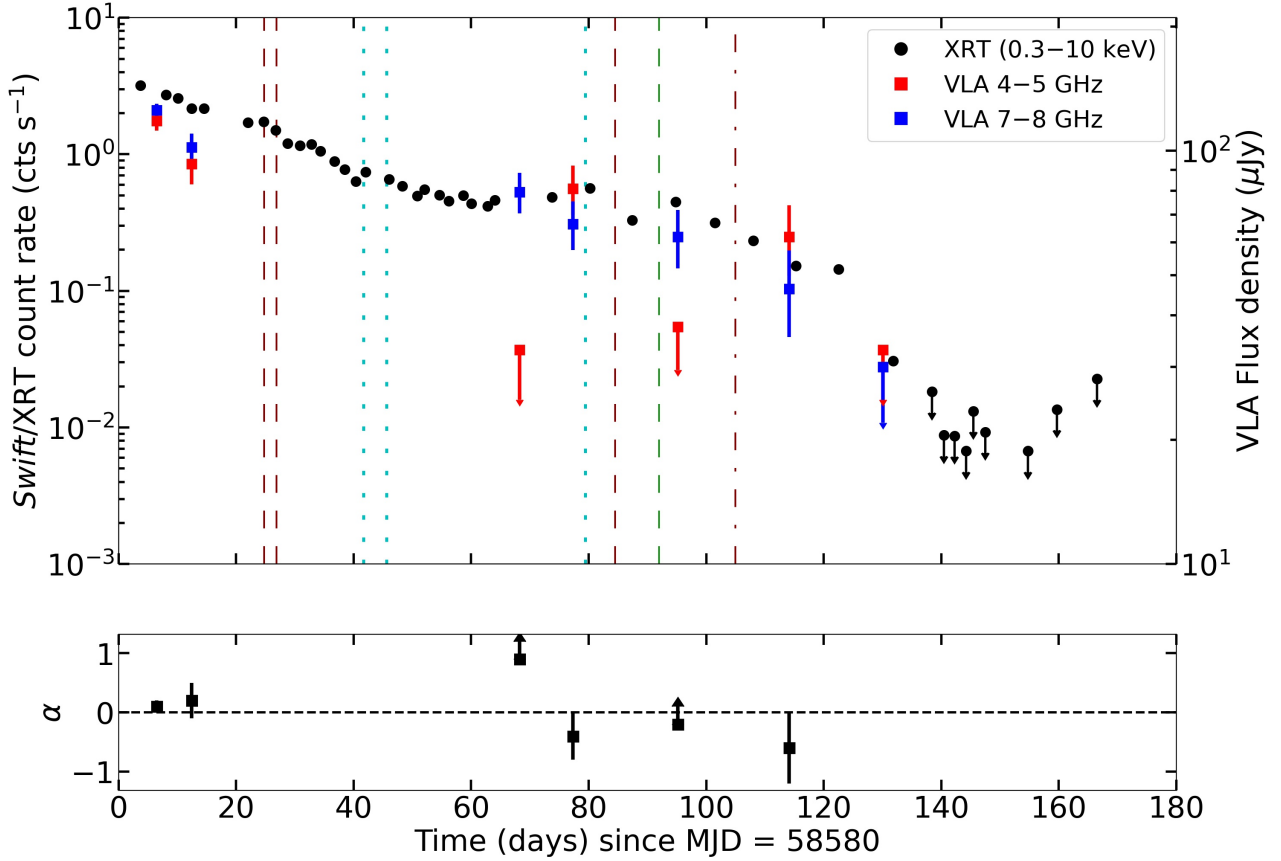
Figure 1. *Top*: X-ray and radio light curve for the 2019 outburst of IGR J17285−2922. The black circles show the *Swift*/XRT count rate, and the red and blue squares show the VLA 4–5 and 7–8 GHz radio flux density, respectively. The SOAR optical epochs are shown with the brown dashed vertical lines, while the GTC optical epoch is shown with the brown dash-dotted vertical line. The optical photometry epochs are shown with the cyan dotted vertical lines. The nIR spectroscopy epoch is shown with the green dashed vertical line. The data of the *Swift*/XRT observations are given in Table 1, while the data of the VLA observations are given in Table 2. *Bottom*: The radio spectral index α for each VLA observation with at least one detection in either the 4–5 or 7–8 GHz subband. Uncertainties on all data are 1σ. Upper and lower limits are 3σ.

(2014), we use an uncertainty of 0.05 and 0.10 dex on L_R and L_X, or keep the statistical uncertainty, depending on which is larger. This is to account for a lack of strict simultaneity and model dependent count rate to flux conversion. The best-fit parameters are $\gamma = 0.4 \pm 0.2/0.3$, $\delta = 0.4 \pm 0.1/0.2$ and $\sigma_\epsilon = 0.1 \pm 0.7/1$, where these uncertainties correspond to the case of 0.05/0.10 dex uncertainties on the luminosities. We can compare this result for γ to the most recently inferred slope of the NS and BH X-ray binary sample by Gallo et al. (2018). Our slope determined here for IGR J17285−2922 ($\gamma = 0.4 \pm 0.2/0.3$) is consistent with the NS X-ray binaries ($\gamma = 0.44^{+0.05}_{-0.04}$) and BH X-ray binaries ($\gamma = 0.59 \pm 0.02$). We note that our correlation for IGR J17285−2922 is measured over a modest range in X-ray luminosity, spanning only ∼ 2 orders of magnitude, with a radio non-detection in the last epoch. Corbel et al. (2013) show that an X-ray luminosity range extending across > 2 orders of magnitude is needed to accurately measure the $L_R − L_X$ correlation index γ. This is reflected in the adopted uncertainties on the luminosities, as using uncertainties of ∼ 0.15 dex or higher results in too poor quality data to constrain the $L_R − L_X$ correlation.

3.3 X-ray spectral evolution

Another diagnostic we can use is the X-ray spectral evolution of IGR J17285−2922 at low X-ray luminosities. Wijnands et al. (2015)

studied the spectral properties of NS and BH X-ray binaries. They found that when using an absorbed powerlaw model to fit X-ray spectra, NS X-ray binaries have a significantly softer spectrum than BH X-ray binaries between 0.5–10 keV X-ray luminosities of 10^{34}–10^{36} erg s^{-1}.

To measure the X-ray fluxes and consequently luminosities, we first determine the best-fitting model to the 0.5–10 keV spectra. We compare the *Swift*/XRT spectra with and without the addition of a blackbody component (BBODYRAD) using an F-test for the first five *Swift*/XRT observations described in Section 2.1 with N_H as a free parameter (FTEST in XSPEC). We use the first five spectra as these have the highest count rate and we expect the blackbody spectral component to be most prominent during this time. In all five observations, we can not prove the inclusion of a blackbody component to be significant at 1σ-confidence. Next, we fixed the temperature of the blackbody component between 0.2 to 2.6 keV with increments of 0.4 keV for all five observations, which shows that the inclusion of a blackbody component is only significant at 1σ-confidence for the third and fifth observation (ObsID 00011303003 and 00011303005). Having no evidence for a blackbody component, we will only use the powerlaw component from now on in all observations.

Having determined what spectral model to use, we measure $N_H = (0.99 \pm 0.05) \times 10^{22}$ cm^{-2} with a simultaneous fit of all *Swift*/XRT
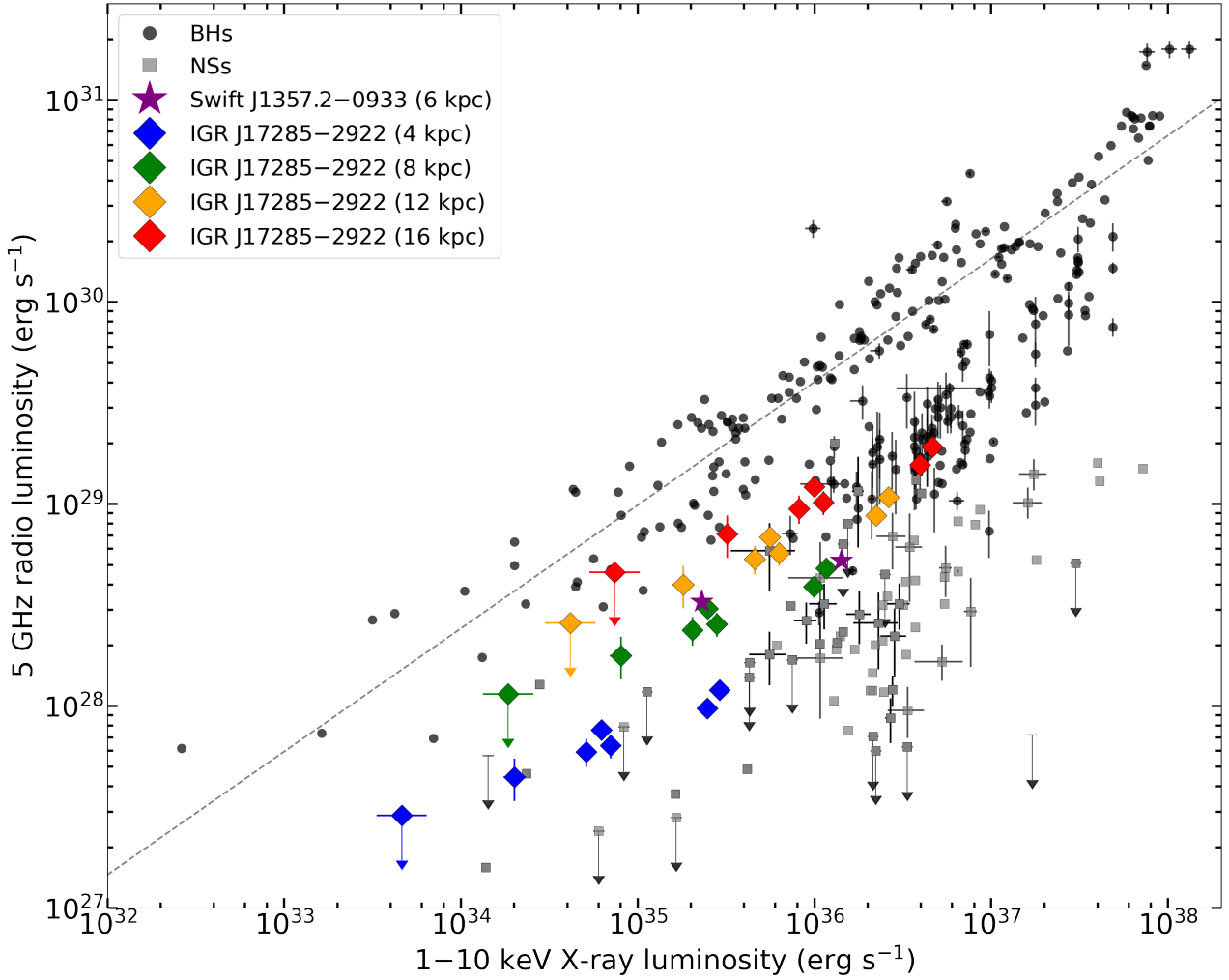
Figure 2. The $L_R - L_X$ plane for X-ray binaries adopted from Bahramian et al. (2018) including the measurements of IGR J17285−2922. We show the $L_R - L_X$ data of IGR J17285−2922 with different colours for the adopted distances of 4, 8, 12 and 16 kpc. We show the BH X-ray binary sample with black circles and the NS X-ray binary sample with gray squares. The dotted black line shows the best-fit relation for BHs as determined by Gallo et al. (2006). We have included two $L_R - L_X$ points for the strong candidate BH (V)FXB Swift J1357.2−0933 for a distance of 6 kpc with purple stars to provide context (Sivakoff et al. 2011; Plotkin et al. 2016; Paice et al. 2019). Uncertainties on all data are 1σ and smaller than their respective marker if they are not shown. Upper and lower limits are 3σ.

spectra with N_H tied for each spectrum. We also determined N_H = $(1.02 \pm 0.03) \times 10^{22}$ cm^{-2} by the weighted least squares of the *Swift*/XRT spectra with N_H as a free parameter for each spectrum. We adopt a fixed N_H of 0.99×10^{22} cm^{-2} in further analysis. We determine 3σ upper limits on the 0.5–10.0 keV unabsorbed flux for the non-detections by scaling the upper limits on the count rate to the count rate of the last detection. We assume that the spectral parameters of the non-detections are equal to that inferred from the last detection. The details of the spectral fits for $N_H = 0.99 \times 10^{22}$ cm^{-2} are listed in Table 1.

We plot in Figure 3 the X-ray power-law index Γ as a function of the 0.5–10 keV X-ray luminosity, using the data in figure 1 of Wijnands et al. (2015), including our results for the 2019 outburst of IGR J17285−2922, assuming a distance of 8 kpc. The evolution of Γ of IGR J17285−2922 seems by eye to be more consistent with the BH X-ray binaries. Wijnands et al. (2015) use a 2D Kolmogorov–Smirnov (KS) to quantify the probability that the two samples are drawn from two different distributions. We find that using a 2D KS test, which uses cumulative distribution functions (CDFs) at its

core, introduces observational biases. An increased density of X-ray observations at a specific time, causes a significantly increased density in the X-ray luminosity space and photon index space. This can significantly alter the CDFs, where they can significantly impact the conclusions.

Since we have a large, not perfectly spaced, number of X-ray observations, we use MC simulations instead of a 2D KS test. For each of the three $\Gamma - L_X$ data sets (NS and BH X-ray binaries, along with IGR J17285−2922), we draw 10^5 data set samples assuming a Gaussian distribution with mean and standard deviation equal to the determined $\Gamma - L_X$ and 1σ errors respectively. Next, we bootstrap these data set samples with replacement obtaining a new data set sample with equal size. We fit to each of these new data set samples the modified linear regression equation

$$\Gamma = a[\log(L_X) - 34] + b \tag{2}$$

to account for a logarithmic X-ray luminosity axis. Here a is the slope of the curve and b is the offset of the curve at $\log(L_X) = 34$, at this value the offset between the NS and BH X-ray binary samples
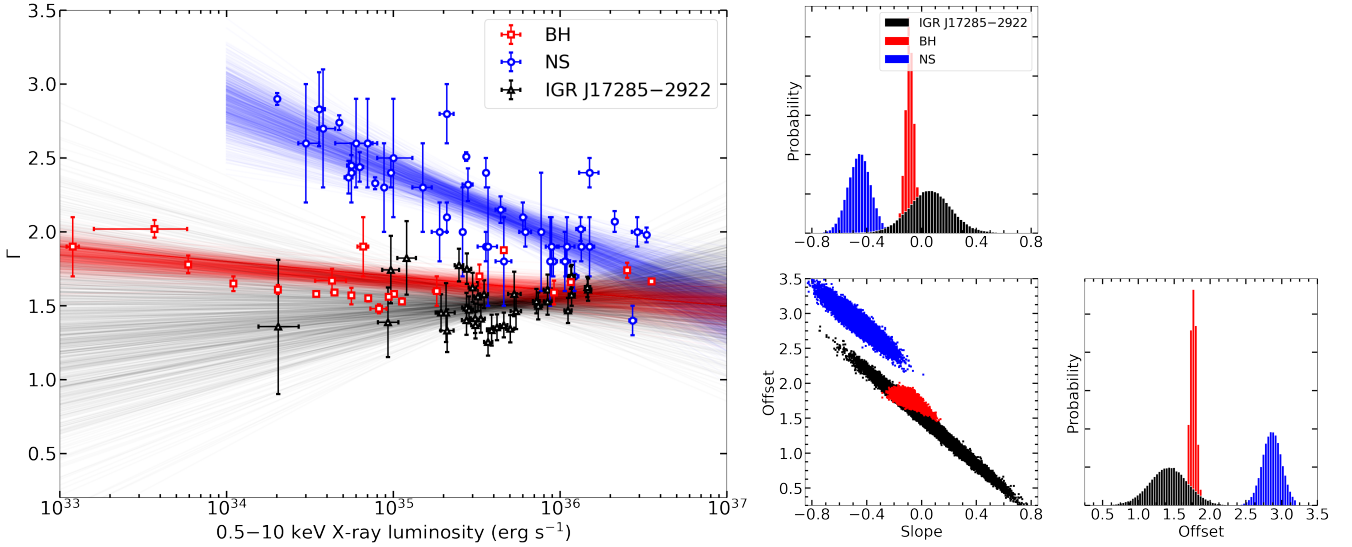
Figure 3. *Left*: X-ray photon index Γ against the 0.5–10 keV X-ray luminosity for BH X-ray binaries (red), NS X-ray binaries (blue) and IGR J17285−2922 (black). We show for each of the three samples the visual representation (cut-off at $L_X = 10^{34}$ for NSs because the NS sample also has this cut-off) of the results of the MC simulations described in Section 3.3 (showing 1/100th of the simulations of each sample to avoid cluttering). The data for the BH and NS sample can be found in Wijnands et al. (2015) and the data for the IGR J17285−2922 sample can be found in Table 1. *Right*: Corner plot of the MC simulations for the slope and offset adopting equal colours as in the *Left* figure.

should be maximally visible. For each of the NS and BH X-ray binaries, and IGR J17285−2922 data sets, the distribution of these slopes and offsets are used to quantify the differences. We have performed these MC simulations for distances of 4, 8, 12 and 16 kpc. We show a visualisation and corner plot of the MC simulations for a distance of 8 kpc in Figure 3. The NS visualisation is cut-off at $L_X = 10^{34}$ because the NS sample itself also has this cut-off in Wijnands et al. (2015). We find that the NS and BH X-ray binary samples are different at 3σ-confidence. For distances of 4, 8, 12 and 16 kpc, the IGR J17285−2922 samples are found to be different from the NS X-ray binary sample at 2σ-confidence in all cases, while the IGR J17285−2922 samples are not found to be different from the BH X-ray binary sample at even 1σ-confidence in all cases. Our X-ray spectral analysis thus favours IGR J17285−2922 having a BH primary rather than a NS primary.

3.4 X-ray light curve fitting

Now that we have investigated the nature of the compact object in IGR J17285−2922 via the $L_R − L_X$ plane and the X-ray spectral evolution at low X-ray luminosities, we move on to investigate the binary parameters. In particular, we are interested in the P_{orb} of the binary system. Heinke et al. (2015) have used the light curves of two VFXBs to estimate P_{orb}. This method is based on the analytical expressions derived by King & Ritter (1998) that explain the shape of the outburst light curve of a typical transient X-ray binary. The overall shape of the light curve is described by an exponential decay above a 'transition' luminosity L_t, below which the shape of the light curve can be described by a linear decay. In physical terms, the exponential decay arises from an entirely ionized disc due to irradiation by the central X-ray source. After irradiation is no longer able to ionize the outer edge of the disc, a linear decay sets in. We can use this transition and the exponential decay to constrain the outer disc radius.

The light curve shape described in the previous paragraph is visible in Figure 1, as IGR J17285−2922 during this 2019 outburst

starts off with an exponential decay followed by a linear decay, where the plateau could be identified as a transition. We can fit [see Powell et al. (2007) and Heinke et al. (2015) for a detailed description] the exponential decay part of this light curve with

$$F(t) = (F_t - F_e)\exp(-\frac{t - t_t}{\tau_e}) + F_e. \qquad (3)$$

Here, F_t is the transition flux at which the light curve changes shape from an exponential to a linear decay. F_e is the limit of the exponential decay, τ_e is the time scale of the exponential decay, and t_t is the time of the transition. We can fit the linear decay part of the light curve with

$$F(t) = F_t \left(1 - \frac{t - t_t}{\tau_l}\right), \qquad (4)$$

with τ_l the time scale of the linear decay. The results of the exponential into linear decay fit are given in Table 3, with the 0.5–10 keV fluxes of the 2019 outburst of IGR J17285−2922 given in Table 1. The 1σ errors on the parameters are determined with an MCMC simulation, for which we give the corner plot in Appendix A. We show the fit to the light curve, along with the residuals in Figure 4.

The disc outer radius R_0 is given by

$$R_0 = \sqrt{3\nu\tau_e} = 3.5 \times 10^7 \sqrt{\tau_e}, \qquad (5)$$

with ν the viscosity (we assume $\nu = 4 \times 10^{14}$ cm^2 s^{-1} following Powell et al. 2007). The transition radius R_{disc} can be derived from the transition flux using

$$R_{disc} = (\phi_H L_t)^{7/12} = (6.4\pi \times 10^{-18} d^2 F_t)^{7/12}. \qquad (6)$$

Here, ϕ_H relates to the amount of matter available for accretion in the disc and accounts for how the disc is irradiated, recalibrated by Heinke et al. (2015) to be $\phi_H = 1.6 \times 10^{-18}$ cm$^{12/7}$ s erg^{-1}. Finally, we can estimate P_{orb} with

$$P_{orb} = 3 \left(\frac{R_{circ}}{R_\odot}\right)^{3/2} \frac{1}{(1 + q)^2} \frac{1}{[0.500 - 0.227\log(q)]^6} h, \qquad (7)$$

where R_{circ} is the circularisation radius and q is the mass ratio
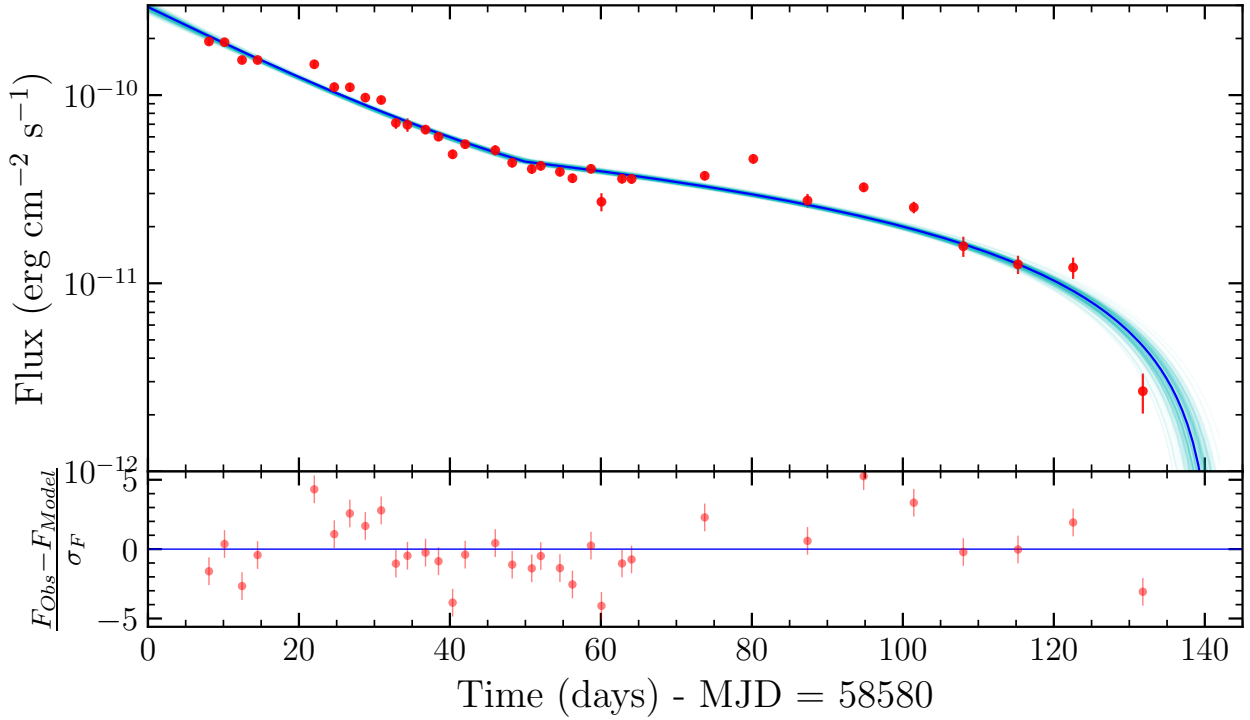
Figure 4. *Top*: The X-ray flux light curve of the 2019 outburst of IGR J17285−2922 indicated with the red circles. The light curve has been fit with an exponential, followed by a linear decay, as described in Section 3.4, indicated by the blue line and blue shaded region. *Bottom*: Residuals for the light curve fit shown in the *top* figure. Uncertainties on all data are 1σ and smaller than their respective marker if they are not shown.

Table 3. Results for the exponential, followed by a linear decay fit, to the light curve of the 2019 outburst for IGR J17285−2922. The orbital period P_{orb} is determined as described in Section 3.4. We give, where possible, the results for CXO J174540.0−290005 and XMM J174457−2850.3 calculated from Heinke et al. (2015). Uncertainties for IGR J17285−2922 are 1σ, while uncertainties for CXO J174540.0−290005 and XMM J174457−2850.3 are 90% confidence, with * representing hard limits reached due to model constraints.

| Source	IGR J17285−2922	CXO J174540.0−290005	XMM J174457−2850.3
F_t (10^{-11} erg s^{-1} cm^{-2})	4.4 ± 0.1	$0.60^{+0.3*}_{-0.03*}$	$1.4^{+0.4}_{-0.8}$
F_e (10^{-11} erg s^{-1} cm^{-2})	$1.9^{+0.2}_{-0.1}$	-	-
t_t (MJD)	58630 ± 1	56447^{+4}_{-5}	54650^{+2*}_{-1*}
τ_e (d)	$20.9^{+0.6}_{-0.7}$	$1.8^{+0.7}_{-0.4}$	$2.4^{+0.1}_{-0.7*}$
τ_l (d)	91 ± 2	8^{+8}_{-6*}	$4.7^{+0.4}_{-2*}$
P_{orb,τ_e} (q=0.1) (h)	9.3 ± 0.2	$1.4^{+0.3}_{-0.3}$	$1.7^{+0.2}_{-0.3}$
P_{orb,L_t} (q=0.1) (h)	$(2.99 \pm 0.06) \times d_{8kpc}^{7/4}$	$0.5^{+0.2}_{-0.1}$	$1.0^{+0.2}_{-0.5}$
P_{orb,τ_e} (q=0.01) (h)	2.17 ± 0.05	-	-
P_{orb,τ_e} (q=0.005) (h)	1.44 ± 0.03	-	-
P_{orb,τ_e} (q=0.001) (h)	0.61 ± 0.02	-	-

between the donor star and compact object (Frank et al. 2002; Heinke et al. 2015). We assume that R_{circ} is given by the disc radius calculated with either Equation 5 (dependent on τ_e) or 6 (dependent on F_t and d).

We give P_{orb} determined with τ_e for a mass ratio $q = 0.1$, 0.01, 0.005 and 0.001 in Table 3. We also give P_{orb} determined with F_t and d for a mass ratio $q = 0.1$ and is consistent with P_{orb} determined with τ_e at a distance of ~ 15 kpc. For a mass ratio $q = 0.001$ we obtain P_{orb} = 0.61 ± 0.02 h, which could suggest that IGR J17285−2922 has an ultra-compact binary orbit. We will further discuss this possibility in Section 4. For comparison, we show the fit results for the two other VFXBs in Table 3, which were proposed to be UCXBs based on the discussed light curve fitting method by Heinke et al. (2015). We note

that the 1σ uncertainties quoted for IGR J17285−2922 are statistical errors and systematic uncertainties introduced in our underlying assumptions can contribute significantly (e.g. differences in R_{disc} and R_{circ} as seen in Powell et al. (2007)).

3.5 Optical photometry

The optical field of IGR J17285−2922 is extremely crowded, and the source was blended with a brighter nearby star on the majority of dates. On three dates under good seeing conditions, the source was automatically detected by the XB-NEWS pipeline and accurate magnitudes could be extracted: $I = 18.24 \pm 0.02$, $I = 18.38 \pm 0.02$, $I = 18.78 \pm 0.01$ on MJD 58621.66, 58625.58 and 58659.42,
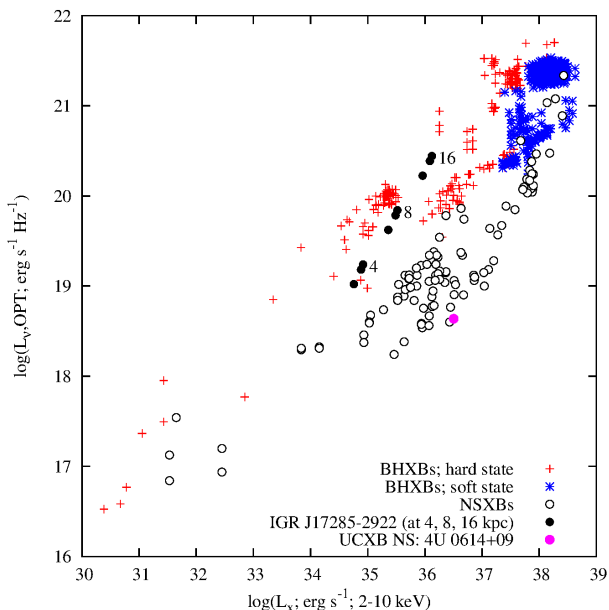
Figure 5. The optical–X-ray luminosity diagram for X-ray binaries with a low-mass donor star, based on Russell et al. (2006) and Russell et al. (2007). Hard and soft state BH X-ray binaries are shown as the red crosses and blue stars, respectively, while NS X-ray binaries are shows as the open circles. IGR J17285-2933 is shown with the black circles for three example distances (4, 8 and 16 kpc), while the NS UCXB 4U 0614+09 is shown in pink.

respectively. We use these accurate measurements in the optical–X-ray correlation diagram in Figure 5. IGR J17285−2922 is shown for three sample distances (4, 8, 16 kpc), alongside a sample of BH and NS X-ray binaries based on Russell et al. (2006) and Russell et al. (2007). For all plotted distances, the optical counterpart of IGR J17285−2922 is consistent with hard state BH X-ray binary systems, while it is between a factor ∼ 5–10 brighter than NS systems.

3.6 Optical spectroscopy

Further evidence in favour of IGR J17285−2922 having an ultra-compact binary orbit comes from our optical spectroscopy around Hα. In Figure 6, we show the four normalized optical spectra taken by GTC and SOAR, where the former is averaged from two spectra taken on the same night. The red-dashed line indicates the Hα rest wavelength, while the blue lines show the rest wavelength of three HeI lines in the bandpass. We have indicated, in grey, telluric and interstellar absorption features. The leftmost band, close to the 5875.6Å HeI line, is the interstellar NaI doublet at 5889 and 5895Å.

No evidence for Hα or He emission is observed in any of the spectra. Therefore, we use the GTC spectrum and MOLLY to measure 3σ upper limits on the equivalent width of four lines, assuming a 2000 km/s velocity width. This yields an equivalent width upper limit of 0.6Å for Hα at 6562.8Å. For the HeI lines, this results in equivalent width upper limits of 0.8Å, 0.6Å, and 0.5Å for the lines at 5875.6Å, 6678.1Å, and 7065.2Å, respectively. For the HeII line at 4686.0Å, we use the two SOAR spectra taken on April 30th and May 2nd, resulting in equivalent width upper limits of 3.7Å and 6.5Å respectively. The Hα upper limit lies below typical equivalent widths seen in both BH and NS X-ray binaries at similar luminosities (see e.g. Fender et al. 2009, for a sample study). Combined, given

these four observations, we do not detect Hα at any point during the outburst. The absence of Hα emission is consistent with the scenario of IGR J17285−2922 having an ultra-compact binary orbit, which would require an hydrogen-poor donor.

3.7 nIR spectroscopy

In Figure 7 we show the K-band segment of the Gemini/Flamingos-2 spectrum of the nIR counterpart to IGR J17285−2922. Much like the optical spectra, the nIR spectrum is featureless and we see no evidence for hydrogen, which is often present as Brγ emission in the nIR spectra of X-ray binaries with low mass donors (e.g. Bandyopadhyay et al. 1997, 1999; van den Berg & Homan 2017). The nIR spectrum does not show any evidence for lines that might be associated with a late-type (main sequence) donor (such as the CO bandheads or neutral metal species such as Al or Ti). However, this is perhaps not surprising considering that the source was still in outburst at the time the nIR observations were performed.

4 DISCUSSION

We have monitored the 2019 outburst of the (V)FXB IGR J17285−2922 with *Swift*/XRT, VLA, SOAR, GTC, Gemini South telescope and LCO telescope network. The *Swift*/XRT spectra are well described by an absorbed powerlaw, indicative of a hard state throughout the outburst. The source was detected with *Swift*/XRT as the count rate decreased over the course of ∼ 128 days, after which the source was no longer detected. IGR J17285−2922 was detected in VLA radio observations as well, both at 4–5 and 7–8 GHz in most observations. Only for the third and fifth VLA epoch, the source was detected in the 7–8 GHz subband, but undetected in the 4–5 GHz subband. The radio spectra are consistent with a flat spectrum, with only the third VLA epoch specifically having a strongly inverted spectrum.

IGR J17285−2922 was no longer detected in radio in the last epoch, coinciding with a steep decrease in *Swift*/XRT count rate. Our VLA observations thus suggest that a compact steady jet (see e.g. Fender 2006; Russell et al. 2016) was detected from IGR J17285−2922 throughout most of the outburst (characterized by a flat radio spectrum), while during at least one epoch discrete ejecta might have been launched (resulting in a steep radio spectrum; e.g. Blandford & Königl 1979). The four optical spectra taken throughout the outburst (both SOAR and GTC) do not reveal Hα emission. Similarly, the nIR spectrum taken with the Gemini South telescope shows no Brγ emission. Three optical photometry measurements show detections with I-magnitudes between 18 and 19 mag.

4.1 The nature of the compact object

We can separate the binary properties of IGR J17285−2922 into three different categories; the nature of the compact object, the nature of the optical and nIR emission, and the nature of the orbital properties of the binary system. We will start with the nature of the compact object, which we can constrain using the $L_R − L_X$ and the $L_{opt} − L_X$ planes, and with the photon index in the low X-ray luminosity regime.

Let us first turn to the $L_R − L_X$ diagram, in which the position of IGR J17285−2922 depends on distance. For distances of 8, 12 and 16 kpc in Figure 2, IGR J17285−2922 is consistent with both the NS and BH X-ray binaries. Approaching shorter distances, IGR J17285−2922 becomes more consistent with NS X-ray binaries,
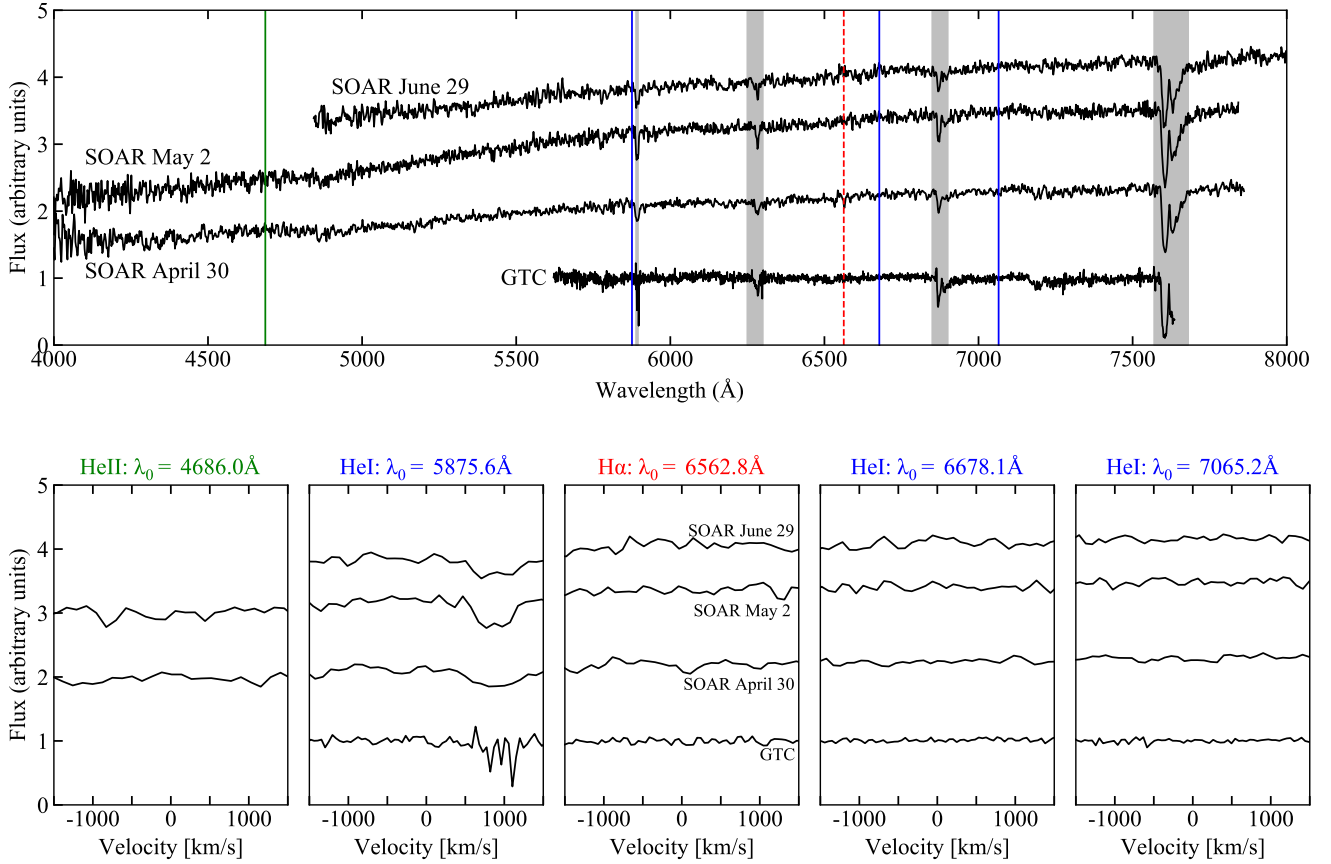
Figure 6. *Top:* optical spectra of IGR J17285−2922, taken with GTC-OSIRIS on July 21–22, 2019 and with SOAR-Goodman Spectograph on on April 30–May 1, May 2–3, and June 29–30, 2019. The GTC spectrum was averaged from two separate spectra taken on the same night. All spectra were renormalized using MOLLY and are plotted with a vertical shift for clarity. The red line indicates Hα, the blue lines show the wavelengths of three HeI lines and the green line shows one HeII line. The grey bands highlight interstellar NaI (left-most) and telluric absorption bands (others). *Bottom:* zoom-in of the four H and He line regions in velocity space, showing how none of these lines are detected in any of the four spectra.

diverging from the BH X-ray binary track. This is visible in Figure 2 for a distance of 4 kpc. Utilizing the $L_R − L_X$ plane to determine the nature of the compact object in an X-ray binary requires careful approach. For a fixed distance, no significance can be given on how much IGR J17285−2922 diverges from either the NS or BH X-ray binaries. Moreover, there are clear outliers such as the radio-bright NS X-ray binary IGR J17591−2342 and the NS candidate X-ray binary 3FGL J0427.9−6704, for which the $L_R − L_X$ location are similar to that of BH X-ray binaries (Russell et al. 2018; Li et al. 2020). In addition, the $L_R−L_X$ correlation for NSs and even BHs are not well established below $L_X \lesssim 10^{36}$ erg s^{-1}. The scarcity in the number of different X-ray binaries at such low X-ray luminosities is a significant caveat. So, the $L_R − L_X$ plane can not be used as an unambiguous differentiator between NS and BH primaries.

In the $L_{opt} − L_X$ plane, BH X-ray binaries show optically brighter counterparts than their NS equivalents (Russell et al. 2006, 2007, see Figure 5). For all trial distances discussed above, IGR J17285−2922 is consistent with a BH system. However, as highlighted as well for the $L_R − L_X$ diagram, at smaller distances than 4 kpc, the system would become more consistent with NS X-ray binaries. While the $L_{opt} − L_X$ plane is better populated down to low X-ray luminosity, especially for NS systems, there is a larger variety of processes possibly contributing to the optical emission.

Therefore, for such small distances, the $L_{opt} − L_X$ diagram would also not be an unambiguous differentiator.

Next, we can use the method developed by Wijnands et al. (2015), which is also dependent on distance but nevertheless yields more conclusive results. The hardness of the X-ray spectra (0.5–10 keV) of IGR J17285−2922 throughout the 2019 outburst in Figure 3 (showing 8 kpc) indicates that a NS X-ray binary can be excluded at 2σ-confidence for all tried distances. This forms a striking contrast with the BH scenario, that is consistent within 1σ for all tried distances. Because the fitted spectral shape is distance independent, only the X-ray luminosity is distance dependent. Changing the distance therefore only affects the offset, as the slope is invariant to the logarithm of a scaling in L_X. It is visible in Figure 3 that the slope is the least constraining parameter. Putting this together, even though the X-ray luminosity is distance dependent, the overall conclusion that the hardness of the X-ray spectra suggest that the compact object in IGR J17285−2922 is a BH remains the same.

Whether the conclusion drawn from Figure 3 is unambiguous and that the conclusion can not be interpreted in any other way remains to be proven, as already mentioned in Wijnands et al. (2015). On top of this, not all X-ray binaries are included with a known Γ and X-ray luminosity between 10^{34} - 10^{36} erg s^{-1}. For example, we have not included the NS X-ray binaries studied in Parikh et al. (2017),
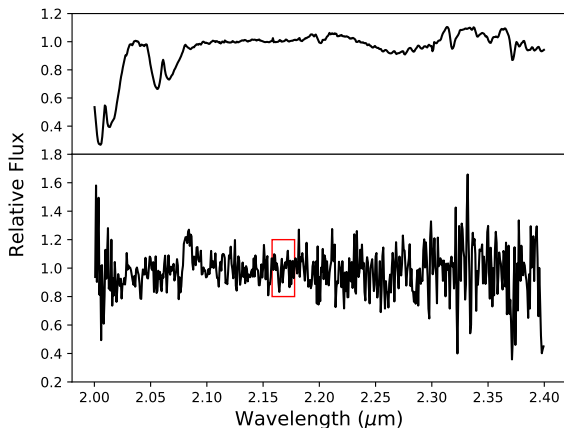
Figure 7. The K-band portion of the Gemini/Flamingos-2 spectrum of the nIR counterpart to IGR J17285−2922. The upper panel shows the telluric transmission spectrum, derived from the standard star Hip 82714, used to correct the target spectrum. The lower panel shows the continuum normalised, telluric corrected spectrum of the target. A red box highlights the region in which we might expect to see Brγ emission. The apparent emission feature between 2.05-2.1 μm is likely a residual from the telluric correction.

which show similar behaviour to the NS X-ray binaries in Wijnands et al. (2015). We have not included the $\Gamma - L_X$ data for EXO 1745−248 studied in Rivera Sandoval et al. (2018), which shows hard X-ray spectra ($\Gamma \sim 1.4$) at quiescent / low X-ray luminosity. Increasing the sample of different NS and BH X-ray binaries in this low X-ray luminosity regime is required to confirm the validity of using this tool. If IGR J17285−2922 is confirmed to harbour a BH, it would add another system to the still scarce sample of BH X-ray binaries studied at and below an X-ray luminosity of 10^{34} erg s^{-1}.

Combining the conclusions of the $L_R - L_X$ and $L_{opt} - L_X$ plane, and the hardness of the X-ray spectra, it is clear that for distances of 8 kpc or greater, the three methods are consistent with the scenario of a BH as compact object. On the other hand, the hardness of the X-ray spectra rules out the NS scenario with 2σ-confidence. For distances around ~ 4 kpc or shorter, the conclusions on the nature of the compact object become inconsistent. The $L_R - L_X$ plane is more consistent with the NS X-ray binaries, while Figure 3 favours a BH as compact object. In order to prevent this inconsistency, the results suggest that the distance to IGR J17285−2922 favours distances around ~ 4 kpc or larger. This supports the conclusion of Sidoli et al. (2011), who estimated the distance to be larger than 4 kpc based on the non-detection ($R > 21$ mag) of IGR J17285−2922 in an archival optical image.

How does this conclusion on the nature of the compact object of IGR J17285−2922 compare to the previous outbursts? IGR J17285−2922 has not been observed in radio prior to our VLA monitoring, so our conclusions regarding the $L_R - L_X$ plane remain unchanged. IGR J17285−2922 has been studied in X-ray in the two previously detected outbursts (Barlow et al. 2005; Sidoli et al. 2011). Similar to the 2019 outburst, IGR J17285−2922 has always been observed in a hard state in both the 2003 and 2010 outburst, with the photon indices reported consistent with the BH sample in Figure 3. In fact, Wijnands et al. (2015) has already suggested that IGR J17285−2922 might harbour a BH based on the hard spectra at low X-ray luminosities. The compact object in IGR J17285−2922 is therefore consistent with a BH.

4.2 The nature of the optical / nIR emission

Next, we will discuss the nature of the optical / nIR emission in IGR J17285−2922. The averaged spectrum taken with the GTC and SOAR (see Figure 6) show a lack of Hα emission, with a stringent 0.6 Å equivalent width upper limit in the GTC data, indicating that the disc might be hydrogen-poor. We also do not detect any Brγ emission in the Gemini/Flamingos-2 nIR spectrum. This could hint towards an ultra-compact binary orbit, requiring a hydrogen-poor donor star to support mass transfer through Roche-lobe overflow. A lack of Hα emission has been reported previously in several optical spectra of UCXBs (Nelemans et al. 2004; Werner et al. 2006; Nelemans et al. 2006; Hernández Santisteban et al. 2019). We obtain equivalent width upper limits of 0.8Å, 0.6Å, and 0.5Å for the HeI lines at 5875.6Å, 6678.1Å, and 7065.2Å respectively and 3.7Å for the HeII line at 4686.0Å. A lack of He emission may not be representative of the population of UCXBs. While a lack of He emission has been reported in, for example, the UCXB IGR J17062−6143 (Hernández Santisteban et al. 2019), the UCXB XB 1916−05 showed strong He emission lines indicative of a He-rich donor star (Nelemans et al. 2006).

While this creates a consistent picture, a lack of Hα emission does not necessarily confirm that the disc is hydrogen-poor. Several other X-ray binaries (excluding UCXBs) have been observed with and without Hα emission (during the same outburst). First, the strong candidate BH X-ray binary Swift J1357.2−0933 has been observed with and without Hα emission during its 2011 outburst, with the non-detection and detection of Hα separated by only 15 hours (Torres et al. 2011; Milisavljevic et al. 2011; Casares et al. 2011). Second, the strong candidate BH X-ray binary Swift J1753.5−0127 has also been observed with and without Hα emission (Torres et al. 2005; Cadolle Bel et al. 2007; Jonker et al. 2008). Third, a single optical spectrum featured no Hα emission in the candidate BH X-ray binary Swift J1539.2−6227 (Torres et al. 2009; Krimm et al. 2011). Finally, an optical spectrum of the NS X-ray binary 1RXS J180408.9−342058, a candidate UCXB, showed no Hα emission (Baglio et al. 2016; Degenaar et al. 2016). A common denominator in these four X-ray binaries is the Hα non-detection is observed in only one optical spectrum for each X-ray binary.

In the case of IGR J17285−2922, four optical spectra were taken at different times during the 2019 outburst (see Figure 1), all showing a lack of Hα. This provides stronger evidence that the donor star in IGR J17285−2922 is hydrogen poor, compared to the sources mentioned. A detailed comparison of the equivalent width upper limits with other X-ray binaries depends on the source distance, due to a possible anti-correlation between equivalent width and X-ray luminosity (Fender et al. 2009); however, the Hα upper limit lies firmly below usual detections, implying that the non-detection does not arise due to signal-to-noise limits. Therefore, an ultra-compact binary orbit with a hydrogen-poor donor in IGR J17285−2922 offers a viable explanation for the optical spectra.

While the absence of hydrogen might be expected, other elements such as carbon, oxygen, neon or iron could be expected in over-abundance. These over-abundances could be identified, for example, as absorption features in X-ray spectra (see e.g. Armas Padilla & López-Navas 2019). While our *Swift*/XRT X-ray spectra of IGR J17285−2922 are of too poor quality to identify these features, the high quality *XMM-Newton* spectrum obtained by Sidoli et al. (2011) is more promising. As noted by Sidoli et al. (2011), clear negative residual structures remain (see their figure 4) after fitting with an absorbed powerlaw, which were partly attributed to incorrect instrumental modeling. The residual structure around ~ 1

Table 4. Overview of the NS UCXBs and short-P_{orb} BH X-ray binaries used. We give the mass function f_x, inclination i, orbital period P_{orb} and mass ratio q for each source along with the relevant references. We constrain i and q for the listed UCXBs as described in Section 4.3. The values for i and q can be rough estimates for some of the short-P_{orb} BH X-ray binaries, such as the values listed for MAXI J1659−152 and Swift J1357.2−0933, so these should only be indicative.

Source UCXBs	f_x ($\times 10^{-7}$ M$_\odot$)	i (°)	P_{orb} (h)	q ($\times 10^{-2}$)	References
IGR J17062−6143	0.912(2)	19−27.5	0.6328(1)	0.8−1.2	(a)
XTE J1807−294	1.53(9)	18.2−85	0.667902(8)	0.4−1.6	(b)
XTE J1751−305	12.78(3)	30−85	0.707039(1)	0.9−2.0	(c)
XTE J0929−314	2.91(1)	18.2−85	0.7263183(8)	0.5−1.9	(d)
IGR J16597−3704	1.18(3)	18.2−85	0.76619(8)	0.4−1.4	(e)
Swift J1756.9−2508	1.56(3)	18.2−85	0.91170(2)	0.4−1.6	(f)
NGC 6440 X−2	1.6(1)	18.2−85	0.955(9)	0.4−1.6	(g)
Short-P_{orb} BH X-ray binaries	f_x (M$_\odot$)	i (°)	P_{orb} (h)	q ($\times 10^{-2}$)	References
MAXI J1659−152	-	65−80	2.414(5)	~2−6.5	(h)
Swift J1357.2−0933	11.0(2)	$\gtrsim$ 80	2.8(3)	~2−6	(i)
Swift J1753.5−0127	-	-	$\simeq$ 3.24	$\lesssim$ 10	(j)
XTE J1118+480	6.3(2)	68(2)	4.078414(5)	4.35(10)	(k)
GRO J0422+32	1.19(2)	45(2)	5.091840(5)	12(8)	(l)

References: $^{(a)}$(Strohmayer et al. 2018); $^{(b)}$(Markwardt et al. 2003; Kirsch et al. 2004); $^{(c)}$(Markwardt et al. 2002); $^{(d)}$(Galloway et al. 2002); $^{(e)}$(Sanna et al. 2018); $^{(f)}$(Krimm et al. 2007); $^{(g)}$(Altamirano et al. 2010); $^{(h)}$(Kuulkers et al. 2013; Molla et al. 2016; Corral-Santana et al. 2018); $^{(i)}$(Corral-Santana et al. 2013; Mata Sánchez et al. 2015; Charles et al. 2019); $^{(j)}$(Zurita et al. 2008); $^{(k)}$(Torres et al. 2004; Gelino et al. 2006; Petrov et al. 2017); $^{(l)}$(Webb et al. 2000; Gelino & Harrison 2003; Petrov et al. 2017)

keV specifically could also be identified as an absorption feature as a result of an enhanced Ne/O ratio, also seen in other UCXBs (Schulz et al. 2001; Juett et al. 2001; Juett & Chakrabarty 2003). This could provide another piece of evidence in favour of the ultra-compact binary orbit in IGR J17285−2922.

Turning to optical photometry, it is generally unclear whether or not the accretion disc is bright enough to be detected. An $R \sim 19$ mag optical counterpart was identified during the 2010 outburst of IGR J17285−2922 (Russell et al. 2010a,b; Turler et al. 2010). In this work, we report I band detections between 18.24 and 18.78 magnitude. From a comparison with the PanSTARRS Database, we find no quiescent counterpart with at a magnitude limit of $r > 23.2^7$, implying a significant optical brightening during the outburst. However, it still remains unclear how much the accretion disc contributes compared to a possibly irradiated donor star or optical emission from a jet [see e.g. Russell et al. (2006, 2007) for a discussion]. If IGR J17285−2922 is indeed an ultra-compact BH system with a small disk, one might expect the optical emission to lie at lower end of the BH distribution if the optical emission is dominated by the accretion disk. Such an effect is, for instance, observed for the NS UCXB 4U 0614+09, highlighted in pink in Figure 5, which is located on the optically faint end of the NS sample. IGR J17285−2922 is instead not located at a similarly faint position in the BH sample, except for small (< 4 kpc) distances.

Possibly, the jet might contribute up to optical bands, increasing the optical flux, while no or little emission from the disk itself is observed. However, with only r-band detections due to the crowded field of IGR J17285−2922 and therefore no optical spectral constraints, this scenario is difficult to test. A less constraining consis-

tency check can however be obtained from the radio observations: while the optical photometric and radio observations were not taken in coordination, the radio flux densities remained relatively constant between radio epochs 2 and 4 (Figure 1) around 80−100 μJy. Assuming that the jet break frequency lies above the I band, a jet spectral index of $\alpha \sim 0.2$ would be sufficient to explain both the radio and optical fluxes from a single, broad-band jet model. This spectral index is close to the approximately flat radio-to-optical spectra typically observed in BH X-ray binaries (Russell et al. 2006). Hence, the radio and optical data are broadly consistent with a jet contributing significantly to the optical increase, instead of the accretion disk. Considering this, it is not obvious that the lack of lines in the optical spectra of these sources would be a result of the jet dominating the optical emission and washing out any lines. For instance, the strong candidate BH X-ray binary Swift J1357.2−0933 had a very weak radio jet (Sivakoff et al. 2011) and 1RXS J180408.9−342058 is a NS X-ray binary that did not reach the bright X-ray regime (Gusinskaia et al. 2017) where one might expect a jet to contribute significantly to the optical emission (Russell et al. 2007).

4.3 The orbital period and the donor star

Following the discussion on the nature of the compact object and donor star, we will discuss the results of the orbital properties (Section 3.4) for IGR J17285−2922. The overall shape of the light curve can be described by an exponential decay during the first half ($\lesssim$ 58631 MJD) of the 2019 outburst, followed by a linear decay during the latter half ($\gtrsim$ 58631 MJD) as the source becomes quiescent. We list P_{orb} for IGR J17285−2922 obtained from both τ_e and L_t in Table 3. The derived P_{orb} for IGR J17285−2922 from these two methods are consistent with each other (assuming equal q) for a distance of $\sim$ 15 kpc. From now on, we will use P_{orb} derived from τ_e as this is distance independent. In addition to this, we give P_{orb} for the two VFXBs CXO J174540.0−290005 (unknown compact object; Koch et al. 2014) and XMM J174457−2850.3 (confirmed

---

^{7} A nearby $r \sim 22.5$ object is significantly detected in the field of IGR J17285−2922, implying a conservative limit of $r > 22.5$ for the field. For this paper, we instead adopt the general PanSTARRS limiting r-band magnitude of 23.2.

NS; Degenaar & Wijnands 2010; Degenaar et al. 2014) for comparison (Heinke et al. 2015). CXO J174540.0−290005 and XMM J174457−2850.3 have the highest quality light curves of transient VFXBs while also showing a clear exponential and/or linear decay. For IGR J17285−2922, P_{orb} (for equal q) is a factor 6 to 7 higher than CXO J174540.0−290005 and XMM J174457−2850.3, which translates to a significantly larger disc radius and consequently τ_e. At first glance this seems to argue against an ultra-compact nature for IGR J17285−2922, but we will show that this is strongly dependent on the nature of the compact object and the assumed q.

In order to give an estimate of P_{orb}, we first need to determine an accurate range of q in X-ray binaries. We can obtain such constraints on q from both accretion theory and observations of known UCXBs. The mass ratio q can be as high as $\sim 5/6$ for X-ray binaries with a low mass donor star ($\lesssim 1 \, M_\odot$), while above $q = 5/6$ mass transfer is expected to occur in a short-lived unstable runaway reaction until the mass ratio is brought down to $q = 5/6$. To determine a lower limit on q, we can turn to X-ray binaries with extremely low donor star masses. Strohmayer et al. (2018) find observational evidence for an extremely small binary mass function of $f_x = (9.12 \pm 0.02) \times 10^{-8} \, M_\odot$ in the NS UCXB IGR J17062−6143 through the measurement of pulsations. The binary mass function f_x is given by

$$f_x = \frac{M_d^3 \sin^3(i)}{(M_c + M_d)^2} = \frac{(2\pi)^2 [a_c \sin(i)]^3}{G P_{orb}^2}. \tag{8}$$

Here, M_d is the donor star mass, i is the inclination, M_c is the compact object mass, $a_c \sin(i)$ is the projected semi-major axis of the binary orbit and G is the gravitational constant. Aside from IGR J17062−6143, six other NS UCXBs have $a_c \sin(i)$ and P_{orb} determined through the measurement of pulsations. We determine, if not already done in the literature, f_x for these NS UCXBs using Equation 8. We list the seven NS UCXBs for which f_x is determined (or already known) and P_{orb} in Table 4, along with their respective references. For each of these seven NS UCXBs, we can set a reasonable lower and upper limit on the NS mass and inclination i to constrain M_d and consequently q using Equation 8. Here, we use a 1.4 $M_\odot$ NS as the lower limit and 2.0 $M_\odot$ NS as the upper limit (Özel & Freire 2016). To set a lower limit on i, a random distribution of inclination angles gives a 95% probability to observe a system at an inclination above $i \simeq 18.2°$ (lower limit). An upper limit on the inclination can be set if the light curve shows a lack of eclipses and dips at $i < 85°$ (Paczyński 1971). For XTE J1751−305 and IGR J17062−6143, we use the constraints on the inclination known from the literature (Markwardt et al. 2002; Strohmayer et al. 2018).

We give for each of the listed NS UCXB in Table 4 the determined lower and upper limits on both i and q. We show the $P_{orb} - q$ relation of IGR J17285−2922 determined from τ_e, along with the seven NS UCXBs discussed in the previous paragraph in Figure 8. On top of this, we show the $P_{orb} - q$ relation for five BH X-ray binaries, which we discuss in Section 4.4. It is visible that for all seven shown NS UCXBs, mass ratios below $q \sim 0.01$ are realistic to discuss. Calculations and simulations by van Haaften et al. (2012) support these observational results, showing that a 1.4 $M_\odot$ NS primary could have a white dwarf donor star mass as low as 0.0042 $M_\odot$ after 10 Gyr of mass transfer (q $\sim$ 0.003). For a 10 $M_\odot$ BH primary, the white dwarf donor star can reach a mass as low as 0.0026 $M_\odot$ (q $\sim$ 0.0003). We give these values for q as lower limits in Figure 8 in the UCXB regime ($P_{orb} < 90$ min). We show in Table 3 that for a mass ratio q = 0.005, P_{orb} for IGR J17285−2922 can reach as low as 1.44 h. Considering that this is a crude estimation of P_{orb} due to possible systematic uncertainties and that even lower mass ratios are
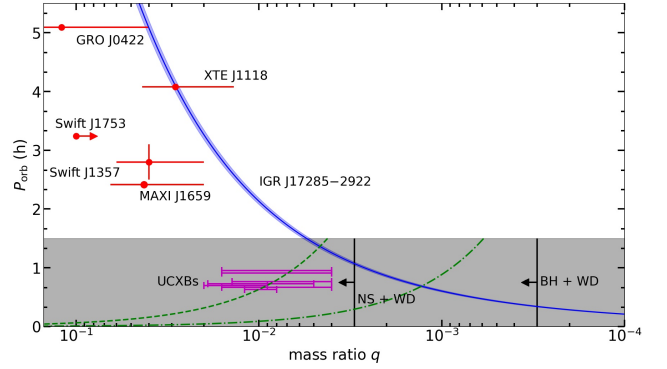
Figure 8. The orbital period P_{orb} as a function of the mass ratio q for IGR J17285−2922 shown with the blue line. We show the region with $P_{orb} < 1.5$ h in gray to highlight the region with UCXBs. The lower limits on q for NS and BH UCXBs are shown in black determined by van Haaften et al. (2012). The analytic approximation of Equation 9 is shown for a 1.4 and 10 $M_\odot$ compact object with the dashed and dash-dotted green curve respectively. The location of seven NS UCXBs with constrained q are shown in magenta. Similarly, the location of five short-P_{orb} BH X-ray binaries with constraints on q are shown in red. The data for the NS UCXBs and the five short-P_{orb} BH X-ray binaries can be found in Table 4.

in theory possible, we can not exclude an ultra-compact nature ($P_{orb} < 90$ min) for both a NS and BH primary. Returning to Table 3, it becomes evident that comparing P_{orb} for IGR J17285−2922 (strongly favours BH primary) to CXO J174540.0−290005 (unknown primary) and XMM J174457−2850.3 (NS primary) for equal q is not trivial if the nature of the compact object differs. As pointed out by van Haaften et al. (2012), the BH UCXBs can probe mass ratios q up to a factor 10 lower than NS UCXBs.

van Haaften et al. (2012) also provide analytic approximations to estimate P_{orb} as a function of the white dwarf donor star mass M_d given by

$$P_{orb} = 0.53 \left(\frac{M_\odot}{M_d} \right) \min = 0.53 \left(\frac{M_\odot}{q M_c} \right) \min, \tag{9}$$

with M_c the mass of the compact object. We show this for compact object masses of 1.4 and 10 $M_\odot$ in Figure 8. The derived donor star masses M_d from P_{orb} in Equation 9 for all seven NS UCXBs are in excellent agreement with their respective M_d constrained from the measurement of pulsations. We can compare Equation 9 to P_{orb} derived from τ_e and q in Equation 7. Under the assumption that the donor star is a white dwarf, we thereby obtain two equations for P_{orb} as a function of q and M_c. Assuming a 1.4 $M_\odot$ NS, these two equations cross at $q \simeq 0.0045$ ($P_{orb} \sim 85$ min). For a 10 $M_\odot$ BH, these two equations cross at $q \simeq 0.0015$ ($P_{orb} \sim 42$ min), supporting the evidence that an ultra-compact binary orbit is possible. This does not directly prove that IGR J17285−2922 is a UCXB, given the possible systematic effects in the method. However, this scenario fits within our observational constraints as discussed here and in Section 4.2.

Almost all known UCXBs have orbital periods shorter than 60 min, with only the UCXB IGR J17494-3030 having an $P_{orb} \sim 75$ min (Ng et al. 2021). Shorter P_{orb} allow, if the system is not persistent, for more frequent outbursts due to a higher $\dot{M}$, increasing the likelihood of observing an outburst, compared to longer P_{orb} (see e.g. Eq. (B.7) in van Haaften et al. 2012). We can estimate the mass-transfer rate (see e.g. Lasota et al. 2008) and compare this to other UCXBs. The three outbursts of IGR J17285−2922 observed

so far in 2003, 2010 and 2019 give an outburst recurrence time scale of ~ 8 yr (Barlow et al. 2005; Sidoli et al. 2011). Integrating the best-fit exponential and linear decay in Section 3.4 over time and allowing for a bolometric correction of 2.9 (in't Zand et al. 2007) gives us a total fluence of $\sim 2 \times 10^{-3}$ erg cm^{-2}. Assuming a distance of 8 kpc and using the recurrence time scale of ~ 8 yr and similar fluence for all outbursts, this implies an $\dot{M} \sim 1 \times 10^{-12}$ M$_\odot$ yr^{-1} (e.g. Eq. (17) in Lasota et al. 2008). Deviations can arise due to uncertainties in recurrence time scale, distance, bolometric correction and fluence estimations for each outburst, so we only use this as an order of magnitude estimate. Comparing the inferred mass transfer rate to for example figure 3 in Lasota et al. (2008), figure 1 in Heinke et al. (2013) or figure 2 in Sengar et al. (2017) shows that IGR J17285−2922 aligns well with the transient UCXB systems at $P_{\rm orb}$ of 50 to 60 minutes. This mass transfer rate also aligns well with the comparison of the light curve fit to the (van Haaften et al. 2012) analytic approximations. The BH UCXB scenario allows for $P_{\rm orb}$ between ~ 40 and 60 min., without invoking an extreme BH mass or mass transfer rate. This is harder to reconcile for the NS UCXB scenario, as it requires $P_{\rm orb}$ between ~ 60 and 90 min., an extremely low mass transfer rate and pushes the theoretical limit for q as we approach lower $P_{\rm orb}$.

4.4 Short-$P_{\rm orb}$ BH X-ray binaries

IGR J17285−2922 has a peak $L_{\rm X} \sim 2 \times 10^{36}$ erg s^{-1} at 8 kpc ($L_{\rm X} \sim 8 \times 10^{36}$ erg s^{-1} at 16 kpc). We have discussed that the nature of the compact object is consistent with a BH. If true, such a low peak $L_{\rm X}$ can not be explained by a magnetically truncated disc as this scenario requires a NS. The optical spectra give strong indications for a hydrogen-poor donor star and the fit to the X-ray flux light curve shows that it is possible for this system to be a UCXB. It has been predicted and shown that the peak luminosity scales with $P_{\rm orb}$ of X-ray binaries (Lasota 2001; Wu et al. 2010). Because UCXBs have $P_{\rm orb} \lesssim 90$ min, these systems could have a low peak $L_{\rm X}$. Currently, all confirmed UCXBs have NS primaries, so while we can not compare IGR J17285−2922 to BH UCXBs, five (strong candidate) BH X-ray binaries are known with a short-$P_{\rm orb}$ ($\lesssim 5$ h), some also showing a low peak $L_{\rm X}$. Shahbaz et al. (2013) show the $P_{\rm orb}$ distribution of BH X-ray binaries (their figure 7), highlighting short-$P_{\rm orb}$ BH X-ray binaries. The distribution shows two distinct clusters around $P_{\rm orb}$ of 8 and 50 h, separated by a possible gap. For any mass ratio $q < 0.1$ which we can expect for a 10 M$_\odot$ BH in an X-ray binary, the orbital period of IGR J17285−2922 is consistent with the cluster around 8 hours and possibly indicative of a short-$P_{\rm orb}$ BH X-ray binary.

We can compare the observed X-ray behaviour of IGR J17285−2922 to short-$P_{\rm orb}$ BH X-ray binaries to further investigate this possibility. Among these sources are Swift J1357.2−0933 (strong BH candidate; Mata Sánchez et al. 2015), XTE J1118+480 (confirmed BH; Gelino et al. 2006), Swift J1753.5−0127 (strong BH candidate; Shaw et al. 2016), MAXI J1659−152 (strong BH candidate; Kuulkers et al. 2013) and GRO J0422+32 (confirmed BH; Gelino & Harrison 2003). First, we can compare the derived $P_{\rm orb} - q$ relation of IGR J17285−2922 to these short-$P_{\rm orb}$ BH X-ray binary systems. We list, if known from the literature, $f_{\rm x}$, i, $P_{\rm orb}$ and q in Table 4 similar to the NS UCXBs discussed in Section 4.3. We note that some of the constraints on i and q for these short-$P_{\rm orb}$ BH X-ray binary systems are (rough) estimates and are not as well constrained as the values listed for the NS UCXBs. These constraints on i and q should only be indicative and should not be taken at face value. Nevertheless, we can include the estimates on

q in Figure 8 for comparison. We can see that the $P_{\rm orb} - q$ relation for IGR J17285−2922 is consistent with the short-$P_{\rm orb}$ BH X-ray binaries.

Second, the donor stars in the short-$P_{\rm orb}$ BH X-ray binaries could be nuclearly evolved stars, having moved off the main-sequence (Haswell et al. 2002; Kuulkers et al. 2013; Shahbaz et al. 2013). Simulations by Pylyser & Savonije (1988) and Ergma & Fedorova (1998) show that these short-$P_{\rm orb}$ BH X-ray binaries, which initially start with a ~ 10 h $P_{\rm orb}$ and $M_{\rm d} \sim 1$ M$_\odot$ can end up with significantly reduced $P_{\rm orb}$ of $\lesssim 5$ h and $M_{\rm d}$ of ~ 0.15 M$_\odot$. These systems can reach such low $P_{\rm orb}$ due to systemic angular-momentum loss accompanied by several Gyr of mass transfer. It is possible for these donor stars to have evolved off the main-sequence, with a significantly low H content ($\sim 0.1-0.2$). The evolutionary calculations by Ergma & Fedorova (1998) also show that it is possible for a BH X-ray binary starting with $P_{\rm orb} \sim 17-22$ hr to evolve to a BH UCXB with $P_{\rm orb} < 1$ hr, starting out with a 1.25 M$_\odot$ donor star and either a 4 or 12 M$_\odot$ BH primary.

Last, the X-ray spectral behaviour of these sources in the low X-ray luminosity regime already match that of IGR J17285−2922, as the BH sample in Figure 3 partly consists of short-$P_{\rm orb}$ BH X-ray binaries and BH X-ray binaries studied in Plotkin et al. (2013). The X-ray spectral behaviour of Swift J1357.2−0933 specifically stands out as this is identical to that of IGR J17285−2922 when fitting *Swift*/XRT data, requiring only an absorbed powerlaw component in a hard state throughout all observed outbursts (Sidoli et al. 2011; Armas Padilla et al. 2013; Beri et al. 2019). The position of Swift J1357.2−0933 for a distance of 6 kpc (Sivakoff et al. 2011; Plotkin et al. 2016; Paice et al. 2019) in the $L_{\rm R} - L_{\rm X}$ plane in Figure 2 is consistent with that of IGR J17285−2922 for a distance of ~ 8 to 12 kpc. Comparing the light curve shape during outburst shows that while the exponential to linear decay transition is clearly seen in IGR J17285−2922, this is not clearly visible in Swift J1357.2−0933. The exponential decay part in the X-ray light curve of Swift J1357.2−0933 (their figure 2; Armas Padilla et al. 2013) could be identified as the monotonically decreasing $L_{\rm X}$. While the linear decay is not clearly visible, it could be identified after the last four or so detections when $L_{\rm X}$ steeply drops and is only constrained through upper limits. This is further supported by the shown UV/optical light curve, which shows a clear correlation to the X-ray light curve and also shows a steeply decreasing magnitude (their figure 2; Armas Padilla et al. 2013). As a first guess, we can estimate $\tau_{\rm e}$ using that $L_{\rm X}$ drops by two orders of magnitude over ~ 150 days monotonically. This results in $\tau_{\rm e} \sim 33$ days, which considering that $P_{\rm orb}$ is known (2.8 ± 0.3 h) for Swift J1357.2−0933 would result in $q \sim 0.01$ from Equation 5 and 7. This is consistent with the previously estimated q for Swift J1357.2−0933 taking into account that this is a first guess, there is an uncertainty in $P_{\rm orb}$ and there are systematic uncertainties. This calculation is done for the 2011 outburst of Swift J1357.2−0933 and is consistent for the 2017 outburst ($\tau_{\rm e} \sim 37$ days from figure 4 in Beri et al. (2019)).

This considers only $\tau_{\rm e}$, but a similar calculation can be done using $L_{\rm t}$. While the transition can not be clearly identified, we can make a reasonable guess at $L_{\rm t} \sim 1.5 \times 10^{33} (d/1.5{\rm kpc})^2$ erg s^{-1} (their figure 2 and table 1; Armas Padilla et al. 2013). For a distance of 6 kpc (Charles et al. 2019) to Swift J1357.2−0933, we would have $L_{\rm t} \sim 2.4 \times 10^{34}$ erg s^{-1}. However, when we now use Equation 6 and 7, we do not converge to a realistic q. To illustrate this, for an assumed $q = 0.1$, we obtain $P_{\rm orb} = 0.3$ h for the given $L_{\rm t}$, with $P_{\rm orb}$ decreasing as q decreases. In order to obtain $q < 0.06$ (Corral-Santana et al. 2013) and $P_{\rm orb} = 2.8$ h, we would need to increase $L_{\rm t}$ by more than a factor of 20 for a distance of 6 kpc. In the case where we assume

P_{orb} = 1.9 hr (3σ lower limit), we would still need to increase L_t by more than a factor of 10 to bring this in line with the upper limit on q.

This discrepancy could be explained by an overall higher intrinsic X-ray luminosity, which would make L_t more in line with the observed P_{orb} and q and to which τ_e is insensitive. This has already been suggested in the literature (see e.g. Corral-Santana et al. 2013; Jiménez-Ibarra et al. 2019; Charles et al. 2019). Although the system was initially thought to be at ∼ 2 kpc, Charles et al. (2019) still require a higher intrinsic X-ray luminosity for a distance of ∼ 6 kpc. Another plausible explanation for this discrepancy is the possibility that the value for ϕ_H recalibrated in Heinke et al. (2015) is significantly larger for Swift J1357.2−0933. This could be similar to XTE J1751−305 and 4U 1543−475, which required ϕ_H to be a factor of ∼ 10 smaller as noted by Heinke et al. (2015). Fitting the X-ray light curve therefore requires a careful approach and the conclusions drawn therefrom should only be indicative. In the case of IGR J17285−2922, the derived $P_{orb} - q$ relation from the τ_e and L_t method are consistent with one another at d ∼ 15 kpc. At this distance, the conclusions drawn from the $L_R - L_X$ and $L_{opt} - L_X$ plane, and X-ray spectral evolution at low X-ray luminosity are also consistent with a BH primary.

4.5   The hydrogen column density N_H

Lastly, we will discuss the inconsistency in the best-fitting N_H determined here and during the 2010 outburst. The best-fitting N_H = (0.99 ± 0.05) × 10^{22} cm^{-2} is determined here with a simultaneous fit of all *Swift*/XRT spectra for the 2019 outburst of IGR J17285−2922. The high quality X-ray spectrum taken with *XMM-Newton* during the 2010 outburst of IGR J17285−2922 shows that the best-fit N_H = (0.510 ± 0.005) × 10^{22}cm^{-2} (Sidoli et al. 2011). Two *Swift*/XRT spectra taken during the 2010 outburst as well are consistent within their 1σ error with the absorption column N_H determined by *XMM-Newton*. Therefore, the N_H determined here for the 2019 outburst and the N_H determined for the 2010 outburst are not consistent with one another (factor 2 difference), even accounting for uncertainties.

To check whether this difference in the absorption column N_H significantly affects our conclusions, we repeated the *Swift*/XRT fits by assuming that the N_H determined by Sidoli et al. (2011) is the correct value, regardless of the goodness of fit. In this case, the *Swift*/XRT spectra are even harder, with photon indices ranging from Γ ∼ 0.9 to 1.6. Similar photon indices were observed in the very hard state of six NS X-ray binaries in Parikh et al. (2017). While five of the six of these NS X-ray binaries in the very hard state followed the NS track, IGR J17285−2922 lies clearly systematically below both the NS and BH tracks. If the N_H determined by Sidoli et al. (2011) is correct, it would suggest a very hard state not observed in other X-ray binaries regardless of the nature of the compact object. However, a similar discrepancy in N_H has already been noted in the X-ray spectral fitting of *Swift*/XRT observations of Aql X-1, but did not alter any conclusions (López-Navas et al. 2020). Parikh et al. (2017) also noted that discrepancies in N_H can arise from differences in assumptions, effects introduced by pile-up and adopted model for *Swift*/XRT observations. We found that not adopting the abundances by Wilms et al. (2000), but instead use the default XSPEC abundances by Anders & Grevesse (1989) can reproduce the N_H measured by Sidoli et al. (2011), who do not quote the abundances and cross-sections used. For these reasons, we deem it justified to use the best-fitting N_H for our analysis and the subsequent conclusions.

5   CONCLUSIONS

We have monitored the 2019 outburst of the (V)FXB IGR J17285−2922 in X-ray with *Swift*, in radio with the VLA, in optical with the GTC and SOAR (spectra) and LCO telescope network (photometry) and in nIR with the Gemini South telescope (spectrum). The location of IGR J17285−2922 in the $L_R - L_X$ plane for tried distances of 4, 8, 12 and 16 kpc is consistent with both the NS and BH X-ray binaries. The location of IGR J17285−2922 in the $L_{opt} - L_X$ plane for tried distances of 4, 8 and 16 kpc is consistent with BH X-ray binaries. From the X-ray photon index Γ in the low L_X regime, we also find evidence that the compact object in IGR J17285−2922 is a BH for distances of 4, 8, 12 and 16 kpc.

With four optical spectra from the GTC and SOAR during this 2019 outburst we find that there is considerable evidence for a hydrogen-poor donor star, as all four optical spectra show no Hα emission. The nIR spectrum taken with the Gemini South telescope also reveals no Brγ emission. The low peak L_X of IGR J17285−2922 and possible hydrogen-poor donor star gives indications of an ultra-compact binary orbit.

The shape of the X-ray light curve can be well described by an exponential, followed by a linear decay. For an assumed $q \lesssim 0.1$, the orbital period of IGR J17285−2922 is consistent with short-P_{orb} BH X-ray binaries. We compare the $P_{orb} - q$ relation for IGR J17285−2922 with seven NS UCXBs with constrained q and theory by van Haaften et al. (2012). This comparison supports the evidence that an ultra-compact binary orbit in IGR J17285−2922 can not be excluded. A determination of the orbital period in IGR J17285−2922 will not only give valuable information on the nature of this system, but will give an estimate on the mass ratio q as well from τ_e.

We have shown here that observing a VFXB outburst with a dedicated multi-wavelength campaign provides invaluable information about the nature of the compact object, donor star and the binary orbit. Reproducing such a multi-wavelength campaign for the outbursts of other VFXBs allows us to understand why the population of VFXBs in general is extremely faint. This in turn is highly warranted to improve our understanding of accretion physics (at low X-ray luminosity), binary- evolution and population synthesis.

DATA AVAILABILITY

The data and data products presented in this paper are available at the following DOI: http://doi.org/10.5281/zenodo.4664505

REFERENCES

Altamirano D., et al., 2010, ApJ, 712, L58
Anders E., Grevesse N., 1989, Geochimica Cosmochimica Acta, 53, 197
Armas Padilla M., López-Navas E., 2019, MNRAS, 488, 5014
Armas Padilla M., Degenaar N., Russell D. M., Wijnands R., 2013, MNRAS, 428, 3083
Arnaud K. A., 1996, XSPEC: The First Ten Years. p. 17
Baglio M. C., D'Avanzo P., Campana S., Goldoni P., Masetti N., Muñoz-Darias T., Patiño-Álvarez V., Chavushyan V., 2016, A&A, 587, A102
Bahramian A., et al., 2017, MNRAS, 467, 2199
Bahramian A., et al., 2018, Radio/X-ray correlation database for X-ray binaries
Bahramian A., et al., 2020, arXiv e-prints, p. arXiv:2009.10322
Bandyopadhyay R., Shahbaz T., Charles P. A., van Kerkwijk M. H., Naylor T., 1997, MNRAS, 285, 718
Bandyopadhyay R. M., Shahbaz T., Charles P. A., Naylor T., 1999, MNRAS, 306, 417
Barlow E. J., et al., 2005, A&A, 437, L27
Belloni T. M., 2010, States and Transitions in Black Hole Binaries. p. 53
Beri A., et al., 2019, MNRAS, 485, 3064
Blandford R. D., Königl A., 1979, ApJ, 232, 34
Burrows D. N., et al., 2005, Space Sci. Rev., 120, 165
Cadolle Bel M., et al., 2007, ApJ, 659, 549
Cartwright T. F., Engel M. C., Heinke C. O., Sivakoff G. R., Berger J. J., Gladstone J. C., Ivanova N., 2013, ApJ, 768, 183
Casares J., Torres M. A. P., Negueruela I., Gonzalez-Fernandez C., Corral-Santana J. M., Zurita C., Llano S. R., 2011, The Astronomer's Telegram, 3206, 1
Cash W., 1979, ApJ, 228, 939
Cepa J., et al., 2000, in Iye M., Moorwood A. F., eds, Society of Photo-Optical Instrumentation Engineers (SPIE) Conference Series Vol. 4008, Proc. SPIE. pp 623–631
Chakrabarty D., Jonker P. G., Markwardt C. B., 2010, The Astronomer's Telegram, 2869, 1
Charles P., Matthews J. H., Buckley D. A. H., Gandhi P., Kotze E., Paice J., 2019, MNRAS, 489, L47
Clemens J. C., Crain J. A., Anderson R., 2004, in Moorwood A. F. M., Iye M., eds, Society of Photo-Optical Instrumentation Engineers (SPIE) Conference Series Vol. 5492, Proc. SPIE. pp 331–340
Corbel S., Nowak M. A., Fender R. P., Tzioumis A. K., Markoff S., 2003, A&A, 400, 1007
Corbel S., Coriat M., Brocksopp C., Tzioumis A. K., Fender R. P., Tomsick J. A., Buxton M. M., Bailyn C. D., 2013, MNRAS, 428, 2500
Corral-Santana J. M., Casares J., Muñoz-Darias T., Rodríguez-Gil P., Shahbaz T., Torres M. A. P., Zurita C., Tyndall A. A., 2013, Science, 339, 1048
Corral-Santana J. M., et al., 2018, MNRAS, 475, 1036
D'Angelo C. R., Spruit H. C., 2010, MNRAS, 406, 1208
Degenaar N., Wijnands R., 2010, A&A, 524, A69
Degenaar N., et al., 2014, ApJ, 792, 109
Degenaar N., et al., 2016, MNRAS, 461, 4049
Degenaar N., Pinto C., Miller J. M., Wijnands R., Altamirano D., Paerels F., Fabian A. C., Chakrabarty D., 2017, MNRAS, 464, 398
Ducci L., Grinberg V., Wilms J., Rodriguez J., Bozzo E., Ferrigno C., Savchenko V., 2019, The Astronomer's Telegram, 12646, 1
Ergma E., Fedorova A., 1998, A&A, 338, 69
Evans P. A., et al., 2007, A&A, 469, 379
Evans P. A., et al., 2009, MNRAS, 397, 1177
Fabian A. C., Rees M. J., Stella L., White N. E., 1989, MNRAS, 238, 729
Fender R., 2006, Jets from X-ray binaries. pp 381–419
Fender R. P., Kuulkers E., 2001, MNRAS, 324, 923

Fender R. P., Russell D. M., Knigge C., Soria R., Hynes R. I., Goad M., 2009, MNRAS, 393, 1608
Frank J., King A., Raine D. J., 2002, Accretion Power in Astrophysics: Third Edition
Gallo E., Fender R. P., Miller-Jones J. C. A., Merloni A., Jonker P. G., Heinz S., Maccarone T. J., van der Klis M., 2006, MNRAS, 370, 1351
Gallo E., et al., 2014, MNRAS, 445, 290
Gallo E., Degenaar N., van den Eijnden J., 2018, MNRAS, 478, L132
Galloway D. K., Chakrabarty D., Morgan E. H., Remillard R. A., 2002, ApJ, 576, L137
Gehrels N., et al., 2004, ApJ, 611, 1005
Gelino D. M., Harrison T. E., 2003, ApJ, 599, 1254
Gelino D. M., Balman Ş., Kızıloğlu Ü., Yılmaz A., Kalemci E., Tomsick J. A., 2006, ApJ, 642, 438
Goodwin A. J., et al., 2020, MNRAS, 498, 3429
Gusinskaia N. V., et al., 2017, MNRAS, 470, 1871
Gusinskaia N. V., et al., 2020, MNRAS, 492, 2858
Hameury J.-M., 2019, arXiv e-prints, p. arXiv:1910.01852
Haswell C. A., Hynes R. I., King A. R., Schenker K., 2002, MNRAS, 332, 928
Heinke C. O., Ivanova N., Engel M. C., Pavlovskii K., Sivakoff G. R., Cartwright T. F., Gladstone J. C., 2013, ApJ, 768, 184
Heinke C. O., Bahramian A., Degenaar N., Wijnands R., 2015, MNRAS, 447, 3034
Hernández Santisteban J. V., et al., 2019, MNRAS, 488, 4596
Illarionov A. F., Sunyaev R. A., 1975, A&A, 39, 185
Jiménez-Ibarra F., Muñoz-Darias T., Casares J., Armas Padilla M., Corral-Santana J. M., 2019, MNRAS, 489, 3420
Jonker P. G., Torres M. A. P., Steeghs D., 2008, in Bandyopadhyay R. M., Wachter S., Gelino D., Gelino C. R., eds, American Institute of Physics Conference Series Vol. 1010, A Population Explosion: The Nature & Evolution of X-ray Binaries in Diverse Environments. pp 109–116 (arXiv:0806.3888)
Juett A. M., Chakrabarty D., 2003, ApJ, 599, 498
Juett A. M., Psaltis D., Chakrabarty D., 2001, ApJ, 560, L59
Kelly B. C., 2007, ApJ, 665, 1489
King A. R., Ritter H., 1998, MNRAS, 293, L42
King A. R., Wijnands R., 2006, MNRAS, 366, L31
Kirsch M. G. F., Mukerjee K., Breitfellner M. G., Djavidnia S., Freyberg M. J., Kendziorra E., Smith M. J. S., 2004, A&A, 423, L9
Koch E. W., et al., 2014, MNRAS, 442, 372
Koliopanos F., Peault M., Vasilopoulos G., Webb N., 2020, arXiv e-prints, p. arXiv:2001.00716
Krimm H. A., et al., 2007, ApJ, 668, L147
Krimm H. A., Tomsick J. A., Markwardt C. B., Brocksopp C., Grisé F., Kaaret P., Romano P., 2011, ApJ, 735, 104
Kuulkers E., et al., 2013, A&A, 552, A32
Lasota J.-P., 2001, New Astron. Rev., 45, 449
Lasota J. P., Dubus G., Kruk K., 2008, A&A, 486, 523
Lewis F., Roche P., Russell D. M., Fender R. P., 2008, in Bandyopadhyay R. M., Wachter S., Gelino D., Gelino C. R., eds, American Institute of Physics Conference Series Vol. 1010, A Population Explosion: The Nature & Evolution of X-ray Binaries in Diverse Environments. pp 204–206 (arXiv:0712.2751), doi:10.1063/1.2945042
Li K.-L., Strader J., Miller-Jones J. C. A., Heinke C. O., Chomiuk L., 2020, ApJ, 895, 89
López-Navas E., Degenaar N., Parikh A. S., Hernández Santisteban J. V., van den Eijnden J., 2020, MNRAS, 493, 940
Maccarone T. J., Patruno A., 2013, MNRAS, 428, 1335
Maccarone T. J., Kundu A., Zepf S. E., Rhode K. L., 2007, Nature, 445, 183
Maccarone T. J., et al., 2015, arXiv e-prints, p. arXiv:1501.02769
Markwardt C. B., Swank J. H., 2010, The Astronomer's Telegram, 2823, 1
Markwardt C. B., Swank J. H., Strohmayer T. E., in 't Zand J. M., Marshall F. E., 2002, ApJ, 575, L21
Markwardt C. B., Juda M., Swank J. H., 2003, IAU Circ., 8095, 2
Masetti N., Orlandini M., Palazzi E., Amati L., Frontera F., 2006, A&A, 453, 295
Masetti N., et al., 2007, A&A, 470, 331

Mata Sánchez D., Muñoz-Darias T., Casares J., Corral-Santana J. M., Shahbaz T., 2015, MNRAS, 454, 2199

Mattana F., Götz D., Falanga M., Senziani F., de Luca A., Esposito P., Caraveo P. A., 2006, A&A, 460, L1

McMullin J. P., Waters B., Schiebel D., Young W., Golap K., 2007, CASA Architecture and Applications. p. 127

Milisavljevic D., Fesen R. A., Parrent J. T., Thorstensen J. R., 2011, The Astronomer's Telegram, 3146, 1

Miller-Jones J. C. A., et al., 2015, MNRAS, 453, 3918

Molla A. A., Debnath D., Chakrabarti S. K., Mondal S., Jana A., 2016, MNRAS, 460, 3163

Muno M. P., Lu J. R., Baganoff F. K., Brandt W. N., Garmire G. P., Ghez A. M., Hornstein S. D., Morris M. R., 2005, ApJ, 633, 228

Narayan R., Yi I., 1994, ApJ, 428, L13

Nelemans G., Jonker P. G., 2010, New Astron. Rev., 54, 87

Nelemans G., Yungelson L. R., Portegies Zwart S. F., 2001, A&A, 375, 890

Nelemans G., Jonker P. G., Marsh T. R., van der Klis M., 2004, MNRAS, 348, L7

Nelemans G., Jonker P. G., Steeghs D., 2006, MNRAS, 370, 255

Nelson L. A., Rappaport S. A., Joss P. C., 1986, ApJ, 304, 231

Ng M., et al., 2021, ApJ, 908, L15

Özel F., Freire P., 2016, ARA&A, 54, 401

Paczyński B., 1971, ARA&A, 9, 183

Paice J. A., et al., 2019, MNRAS, 488, 512

Parikh A. S., Wijnands R., Degenaar N., Altamirano D., Patruno A., Gusinskaia N. V., Hessels J. W. T., 2017, MNRAS, 468, 3979

Petrov V. S., Antokhina E. A., Cherepashchuk A. M., 2017, Astronomy Reports, 61, 377

Plotkin R. M., Gallo E., Jonker P. G., 2013, ApJ, 773, 59

Plotkin R. M., et al., 2016, MNRAS, 456, 2707

Porquet D., Grosso N., Bélanger G., Goldwurm A., Yusef-Zadeh F., Warwick R. S., Predehl P., 2005, A&A, 443, 571

Powell C. R., Haswell C. A., Falanga M., 2007, MNRAS, 374, 466

Pylyser E., Savonije G. J., 1988, A&A, 191, 57

Remillard R. A., McClintock J. E., 2006, ARA&A, 44, 49

Rivera Sandoval L. E., et al., 2018, MNRAS, 479, 2777

Russell D. M., Fender R. P., Hynes R. I., Brocksopp C., Homan J., Jonker P. G., Buxton M. M., 2006, MNRAS, 371, 1334

Russell D. M., Fender R. P., Jonker P. G., 2007, MNRAS, 379, 1108

Russell D. M., Yang Y. J., Patruno A., Degenaar N., Altamirano D., Wijnands R., Lewis F., 2010a, The Astronomer's Telegram, 2827, 1

Russell D. M., et al., 2010b, The Astronomer's Telegram, 2997, 1

Russell T. D., et al., 2016, MNRAS, 460, 3720

Russell T. D., Degenaar N., Wijnands R., van den Eijnden J., Gusinskaia N. V., Hessels J. W. T., Miller-Jones J. C. A., 2018, ApJ, 869, L16

Russell D. M., et al., 2019, Astronomische Nachrichten, 340, 278

Sanna A., et al., 2018, A&A, 610, L2

Schulz N. S., Chakrabarty D., Marshall H. L., Canizares C. R., Lee J. C., Houck J., 2001, ApJ, 563, 941

Sengar R., Tauris T. M., Langer N., Istrate A. G., 2017, MNRAS, 470, L6

Shahbaz T., Russell D. M., Zurita C., Casares J., Corral-Santana J. M., Dhillon V. S., Marsh T. R., 2013, MNRAS, 434, 2696

Shakura N. I., Sunyaev R. A., 1973, A&A, 500, 33

Shaw A. W., Charles P. A., Casares J., Hernández Santisteban J. V., 2016, MNRAS, 463, 1314

Shaw A. W., et al., 2020, MNRAS, 492, 4344

Sidoli L., Paizis A., Mereghetti S., Götz D., Del Santo M., 2011, MNRAS, 415, 2373

Sivakoff G. R., Miller-Jones J. C. A., Krimm H. A., 2011, The Astronomer's Telegram, 3147, 1

Spencer R. E., 1979, Nature, 282, 483

Steele M. M., Zepf S. E., Maccarone T. J., Kundu A., Rhode K. L., Salzer J. J., 2014, ApJ, 785, 147

Strohmayer T. E., et al., 2018, ApJ, 858, L13

Tauris T. M., van den Heuvel E. P. J., 2006, Formation and evolution of compact stellar X-ray sources. pp 623–665

Tetarenko B. E., Sivakoff G. R., Heinke C. O., Gladstone J. C., 2016, ApJS, 222, 15

Torres M. A. P., Callanan P. J., Garcia M. R., Zhao P., Laycock S., Kong A. K. H., 2004, ApJ, 612, 1026

Torres M. A. P., et al., 2005, The Astronomer's Telegram, 551, 1

Torres M. A. P., Jonker P. G., Steeghs D., Chen H. W., Shectman S. A., Floyd D. J. E., 2009, The Astronomer's Telegram, 1958, 1

Torres M. A. P., Steeghs D., Jonker P. G., Ross N. R., 2010, The Astronomer's Telegram, 2870, 1

Torres M. A. P., Steeghs D., Jonker P. G., Rauch M., 2011, The Astronomer's Telegram, 3143, 1

Turler M., et al., 2010, The Astronomer's Telegram, 2825, 1

Verner D. A., et al., 1996, ApJ, 465, 487

Webb N. A., Naylor T., Ioannou Z., Charles P. A., Shahbaz T., 2000, MNRAS, 317, 528

Werner K., Nagel T., Rauch T., Hammer N. J., Dreizler S., 2006, A&A, 450, 725

Wijnands R., et al., 2006, A&A, 449, 1117

Wijnands R., et al., 2015, MNRAS, 454, 1371

Wilms J., et al., 2000, ApJ, 542, 914

Wu Y. X., Yu W., Li T. P., Maccarone T. J., Li X. D., 2010, ApJ, 718, 620

Yang Y. J., Patruno A., Degenaar N., Russell D. M., Altamirano D., Wijnands R., 2010, The Astronomer's Telegram, 2824, 1

Zepf S. E., et al., 2008, ApJ, 683, L139

Zurita C., Durant M., Torres M. A. P., Shahbaz T., Casares J., Steeghs D., 2008, ApJ, 681, 1458

in't Zand J. J. M., Jonker P. G., Markwardt C. B., 2007, A&A, 465, 953

van Haaften L. M., Nelemans G., Voss R., Wood M. A., Kuijpers J., 2012, A&A, 537, A104

van den Berg M., Homan J., 2017, ApJ, 834, 71

van den Eijnden J., et al., 2018, MNRAS, 475, 2027

van den Eijnden J., Degenaar N., Russell T. D., Hernández Santisteban J. V., Wijnands R., Miller-Jones J. C. A., Rouco Escorial A., Sivakoff G. R., 2019, MNRAS, 483, 4628

APPENDIX A: X-RAY LIGHT CURVE FIT

This paper has been typeset from a TEX/LATEX file prepared by the author.
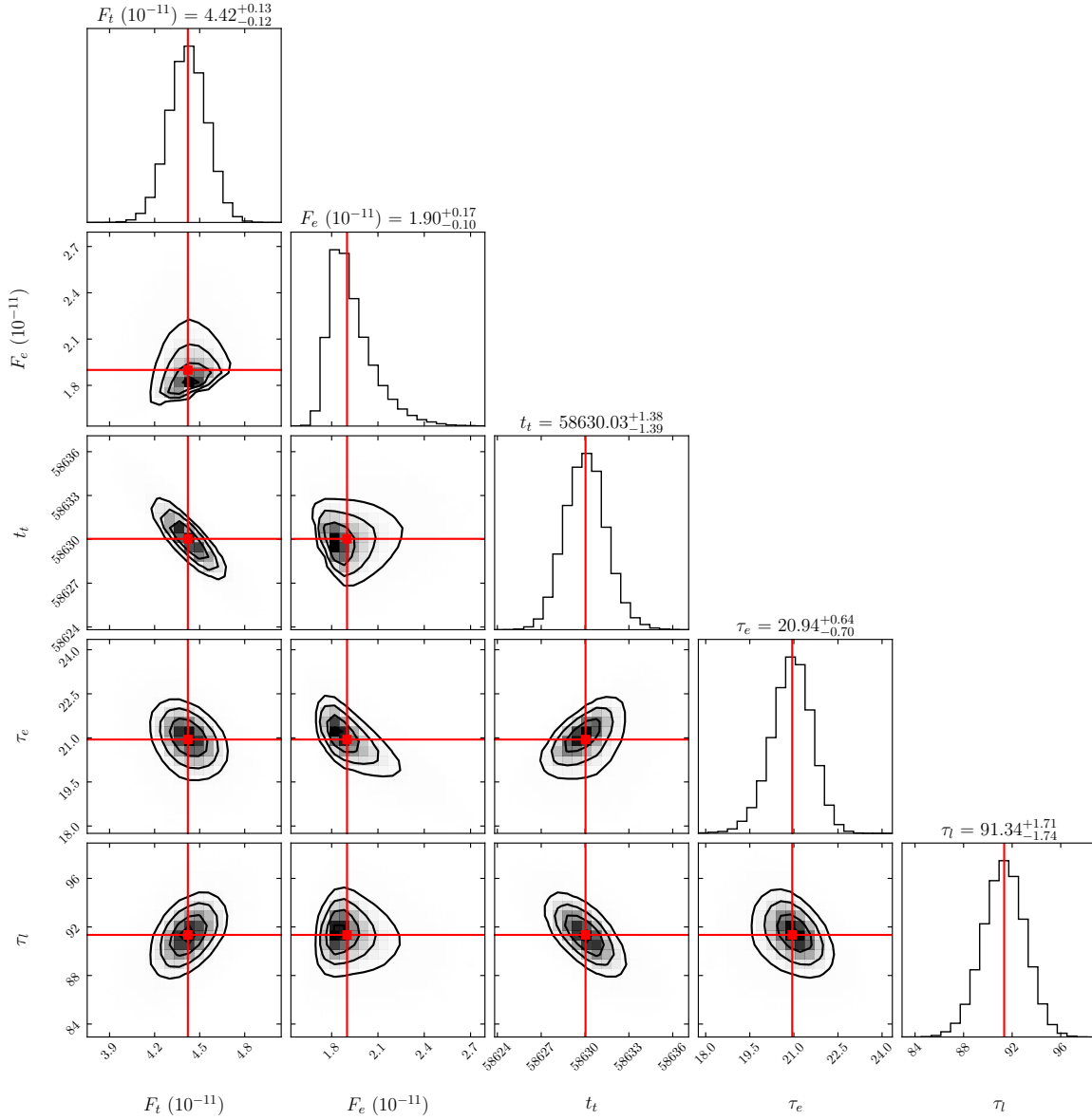
Figure A1. Corner plot for the Monte-Carlo Markov-Chain simulations of the simultaneous exponential and linear decay fit described in Section 3.4. We determine the value for each parameter along, with the negative and positive 1σ error as the 50th, 16th and 84th percentile respectively. $F_{\rm t}$ and $F_{\rm e}$ are given in 10^{-11} erg s^{-1} cm^{-2}, $t_{\rm t}$ is given in Modified Julian Date, and $\tau_{\rm e}$ and $\tau_{\rm l}$ are given in days.